The color of electronic correlation in rare-earth nickelates

RUPPEN, Julien

Abstract

Dans ce travail de thèse, je me suis intéressé à comprendre les aspects de la corrélation électronique tels qu'ils se manifestent dans les nickelates de métaux de transition (TMO). Cette famille de composés possède des caractéristiques intéressantes pour l'étude des phénomènes corrélés à savoir : des transitions de phases électroniques qui s'opèrent par un changement de température. Ceci facilite grandement leur étude par rapport à d'autres composés dont les transitions de phase se font par dopage car leur identité chimique reste inchangée durant la transition et l'on peut donc exclure la contribution des impuretés ou des défauts de cristallisation lors de l'apparition des phénomènes observés. Dans les nickelates de terre rare, nous avons au moins trois régimes identifiés. La phase isolante-antiferromagnétique (AFM), la phase isolante paramagnétique (PM) ainsi que la phase métallique- paramagnétique. L'objet de mon travail de thèse est de donner une explication du spectre optique observé à l'aide de la spectroscopie ellipsométrique. A cette fin, j'utilisais le formalisme de [...]

UNIVERSITÉ
DE GENÈVE

UNIVERSITÉ DE GENÈVE

Department of Quantum Matter Physics

FACULTÉ DES SCIENCES

Professeur Dirk van der Marel

The Color of Electronic Correlation in Rare-Earth Nickelates

THÈSE

présentée à la Faculté des Sciences de l'Université de Genève
pour obtenir le grade de docteur ès Sciences, mention Physique

par

Julien Ruppen

de

Sierre (Suisse)

UNIVERSITÉ DE GENÈVE

FACULTÉ DES SCIENCES

DOCTORAT ÈS SCIENCES, MENTION PHYSIQUE

Thèse de Monsieur Julien RUPPEN

intitulée :

«The Color of Electronic Correlation in Rare-Earth Nickelates»

La Faculté des sciences, sur le préavis de Monsieur D. VAN DER MAREL, professeur ordinaire et directeur de thèse (Département de physique de la matière quantique), Monsieur S. GARIGLIO, docteur (Département de physique de la matière quantique), Monsieur C. BERNHARD, professeur (Département de physique), autorise l'impression de la présente thèse, sans exprimer d'opinion sur les propositions qui y sont énoncées.

Genève, le 7 octobre 2019

<div style="border:1px solid">

Thèse - 5395 -

</div>

Le Doyen

Je dédie ce travail à mon directeur de thèse, Dirk van der Marel, pour sa patience, sa gentillesse et pour son Amour de la Nature.

Abstract

Dans ce travail de thèse, je me suis intéressé à comprendre les aspects de la corrélation électronique tels qu'ils se manifestent dans les nickelates de métaux de transition (TMO). Cette famille de composés possède des caractéristiques intéressantes pour l'étude des phénomènes corrélés à savoir : des transitions de phases électroniques qui s'opèrent par un changement de température. Ceci facilite grandement leur étude par rapport à d'autres composés dont les transitions de phase se font par dopage car leur identité chimique reste inchangée durant la transition et l'on peut donc exclure la contribution des impuretés ou des défauts de cristallisation lors de l'apparition des phénomènes observés. Dans les nickelates de terres rares, nous avons au moins trois régimes identifiés. La phase isolante-antiferromagnétique (AFM), la phase isolante paramagnétique (PM) ainsi que la phase métallique-paramagnétique. Certain de ces composés passent par une seule transition: de la phase isolante AFM à la phase métallique PM. D'autre passent par deux transitions à des températures distincts. D'abord une transition de phase magnétique (MPT) puis une transition de phase métal-isolant (MIT). Nos échantillons ont été préparés au sein du laboratoire du professeur Jean-Marc Triscone. Ils se présentent sous la forme de couches minces de nickelate déposées sur un substrat par une technique de sputtering. Les couches ainsi formées sont monocristallines et entièrement contraintes par le substrat. La surface offerte par ces échantillons est importante et permet d'avoir recours à la spectroscopie pour les caractériser. Ainsi, afin de sonder la structure électronique de nos matériaux, j'utilisais la spectroscopie ellipsométrique. Cette méthode de mesure donne accès directement à la constante diélectrique complexe du matériau. J'opérais des mesures en température afin de sonder toutes les transitions de phase connues. A cette fin, j'utilisais un cryostat dans lequel l'échantillon est refroidit à l'aide d'hélium liquide. Un vide poussé à été réalisé afin d'éviter la condensation de gaz sur l'échantillon. La première observation faite lors de ces mesures est la suivante : la phase isolante, qu'elle soit AFM ou PM, présente un double pic dans sa conductivité optique dans le proche-infrarouge entre 0.5 et 1.5 eV. Ces deux transitions disparaissent dans la phase métallique et ce, dans chacun de nos trois échantillons. Une seconde observation est que la transition entre les phases métalliques et isolantes n'est

pas de même nature dans tous nos échantillons. Alors qu'elle est de type premier ordre dans les matériaux ayant une seule transition de phase, elle est du type second ordre dans les matériaux présentant deux transitions distincts. Enfin, dans ces derniers matériaux, l'on peut faire l'observation remarquable d'un "coude" dans la trace en température de la conductivité optique aux alentours de la température de Néel. L'objet de mon travail de thèse consiste donc à donner une explication à chacune de ces trois observations. A cette fin, j'utilisais le formalisme de Ginzburg-Landau ainsi que, en collaboration avec le professeur Antoine Georges et son équipe, des calculs numériques implémentant la DMFT. Notre point de départ pour la représentation de la structure électronique de ces matériaux repose sur l'idée, par ailleurs solidement confirmée par de nombreuses expériences, qu'il existe deux types de nickel différents au sein des nickelates. Chacun de ces deux nickel est dans une configuration d^8 mais seulement un nickel sur deux forme un état lié avec des trous provenants du ligand oxygène. L'existence de ces trous est dû au transfert d'électron de oxygène au métal de transition. En conséquent, il existe une certaine hybridation entre les états 3d du nickel et les états 2p de l'oxygène. Ce sont donc des états hybridés qui donnent lieu au spectre observé. Les calculs ab-initio basés sur ce modèle reproduisent correctement les deux pics observés entre 0.5 et 1.5 eV. La transition de plus faible énergie correspond à une transitions de part et d'autre du gap de Mott. Les calculs montrent qu'un second "pseudo-gap" s'ouvre au sein des états vacants de Hubbard. Il s'agit d'un pseudo-gap de Peierls dont les états "vacants" ont un caractère fortement hybridé avec les trous du liguant. La deuxième transition observée expérimentalement se produit depuis les états occupés de Hubbard vers ces états. En ce qui concerne le "coude" visible sur la trace en température de la conductivité optique, l'approche phénoménologique basé sur la théorie de Ginzburg-Laundau nous permet de donner l'explication suivante : Il existe un couplage entre deux phases présentes au sein des nickelates. Chacune de ces phases est représentée par un paramètre d'ordre, lequel contribue à l'énergie totale du système. L'une de ces phases est associée au degrés d'asymétrie entre les deux types de nickel alors que la deuxième phase est représentée par la magnétisation du système. Un couplage du type bi-quadratique entre les deux paramètres d'ordre associés à chacune de ces phases permet de reproduire le "coude" observé aux alentours de la température de Néel. La possibilité d'un tel couplage est renforcée par le fait que l'intensité du double pic augmente dans la phase AFM. Bien que l'interprétation microscopique de ce phénomène soit toujours manquante, on peut dorénavant affirmer que l'ordre de charge couple avec l'ordre magnétique dans les nickelates de terres-rares.

Contents

Chapter 1

Motivation of this research

According to the band theory of solids, each electron interacts with a static potential which is formed by the fixed nucleus as well as the averaged positions of all other electrons. There is no feedback from one electron to another. Correlation effects are replaced by an effective one-particle potential, which greatly simplifies the computation of the available energy levels in a given system. The quantum states of each energy level are determined by a linear combination of all states available at a given energy level. Using this approximation, systems with a large number of electrons can be tackled. The physics of independent electrons provides a solid framework for understanding many properties such as electrical and thermal conductivity, optical absorption, ductility or magnetic susceptibility.

The study of systems such as NiO however, show that the single electron approximation is insufficient to capture the physics of every material [1]. In a Mott insulator, the Coulomb interaction is strong enough to dictate new dynamics in which electrons are confined by their interactions with others. Itinerancy drastically reduces and the system becomes insulating when it should be metallic according to the band theory. The discovery of superconductivity in oxide [2] further confronted the scientific community with the necessity of a new model for electron dynamics.

Many unexpected properties emerge from the interplay between electrons. Colossal magnetoresistance, multiferroicity and metal-insulator transition are among the many macroscopic manifestations of the electronic correlation which occur in the transition metals and their compounds (TMC). There are significant challenges to understanding these materials, and there is an important industrial impact regarding the ability to synthesize or design high-temperature superconductors. There are other properties of correlated materials with interesting technical applications and potential economic impact. However, there are limitations without better understanding the underlying physical principles. Electronic correlations take different forms: The electrostatic interaction (Coulomb) and the Pauli exclusion principle give rise to the exchange interaction as well as spin interaction as revealed by Hunds rules. Other types of correlation

exist such as electron-phonon or spin-orbital. Such interactions are effective in every material but are particularly strong in TMC.

The samples used in this study are epitaxially grown ultra-thin films of TMC on various different substrate materials, synthesized in the group of professor J-M Triscone. The principles of electronic correlation are understood to some extent but a complete landscape of this type of interaction is still lacking. In this thesis, I describe the experiments performed using spectroscopic ellipsometry on Rare-Earth (RE) nickelates within a temperature range allowing the occurrence of both the metal-insulator and the magnetic phase transition which allowed us to observe the change in dynamics in these systems. We explained the obtained spectra as well as their temperature dependence in the context of dynamical mean field theory. Our goal was to provide details concerning how the lattice, charge and spin degrees of freedom interact.

Nickel in the metallic state of Rare-Earth (RE) nickelates is in the formal electronic configuration $3d^7$ which corresponds to the nominal valence 3+. Stabilizing the Ni^{3+} valence in the $RNiO_3$ structure requires extreme conditions which was accomplished for the first time using high temperature and high pressure [3]. Further improvements of the initial technique were achieved [4] but the single crystals obtained in this manner remain quite small (100 μm). Nickelate single crystals were first obtained without needing high temperature pressure via pulsed laser deposition [5] and chemical vapor deposition [6] on a perovskite oxide substrate with a similar structure. Growing nickelate thin-films under low pressure is possible due to their epitaxial stabilization on perovskite substrates. Epitaxially induced biaxial strains may act as a substitute for the high pressure required to stabilize these oxides [7].

If a substrate stabilizes the nickelate structure, it also influences its properties [8]. The metal-insulator transition temperature (T_{MIT}) for instance is higher when the strain imposed by the substrate is tensile. On the other hand, a compressive strain has an opposite effect on the transition temperature. A possible explanation for this behavior was offered by J-M Triscone et al. [9] who explained the change of T_{MIT} in terms of density of defects. Tensile strains favor Ni^{2+} because this larger ion can accommodate the larger square (planar) unit cell. In order to maintain electro neutrality, defects such as oxygen vacancies appear and the resulting higher defect density then creates a more resistive crystal. For this reason, T_{MIT} will increase. A more reasonable assumption regards so-called bandwidth tuning which involves band overlapping as a function of Ni-O-Ni angles. For small angles, the overlap between nickel and oxygen orbitals is weak and the system is insulating, as represented in Figure 4.3. Such a situation occurs when the central Rare-Earth ion is small. For larger RE ions, this angle increases. The overlap of nickel and oxygen states is then larger and drives the system toward a more metallic state.

Films were deposited on various substrates by either chemical vapor deposition (CVD) or physical vapor deposition (PVD). More details can be found about the deposition process in [9]. The samples under study consist of thin-films of RE nickelate ($NdNiO_3$ and $SmNiO_3$) deposited on 0.5 mm thick substrates. Film thickness varies from 10 to 30 nm and is always small enough
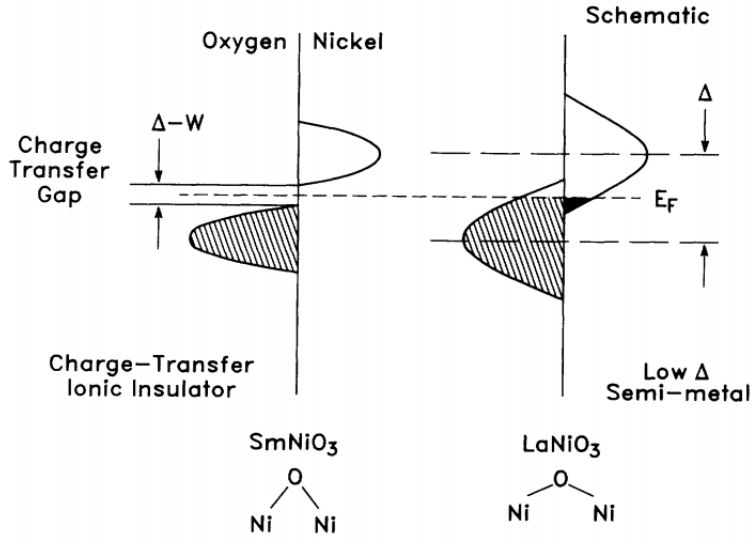
Figure 1.1: Figure from J.B. Torrance [10]. Bandwidth Overlap

Film thickness	Substrate thickness	Stress	Film T_{IMT}/T_{MPT}	Bulk [11] T_{IMT}/T_{MPT}
NNO 30 nm	NGO110 0.5 mm	Tensile	170/170	200/200
NNO 17 nm	NGO101 0.5 mm	Tensile	300/200	200/200
SNO 10 nm	LAO001 0.5 mm	—	350/200	400/200

Table 1.1: Summary of the three different studied systems. The magnetic phase transition (MPT) and the insulator-metal transition (IMT) temperature are in Kelvin. Substrate crystal orientations are in orthorhombic notation.

to ensure monocrystallinity and homogeneous strains.

For this study, we used three different samples: two neodymium nickelate (NNO) and one samarium nickelate (SNO) One NNO thin film is grown on (110) oriented neodymium gallate (NNO/NGO-110) and another is grown on (101) oriented NGO substrate (NNO/NGO-101) Finally, SNO is grown on a (001) oriented lanthanum aluminate (SNO/LAO-001) substrate.

Chapter 2

Experimental methods

In this chapter I describe the principles of modern ellipsometry and the best conditions for optimal measurement. I also describe how we used a cryostat in order to characterize our samples both regarding frequency and temperature.

2.1 Coupling of light and matter

In optics, the response of a material to an electromagnetic field is of interest. In this study we consider only the electric component of light. Light-matter interaction is understood classically in terms of the Drude-Lorentz model which describes how matter responds to light in terms of classical oscillators. An electromagnetic wave propagates into a material by coupling to its charge oscillations. A charge moving out of its equilibrium position creates an electric dipole.

The ease of a material of becoming polarized by an electric field is quantified by a physical quantity called the electric susceptibility χ_e. The larger the susceptibility, the easier it is to polarize the medium in which the light propagates. Electric susceptibility depends on the presence of 'polarization modes'. For this reason, in a given material, χ_e is frequency dependent and enters the expression of a more widely used physical constant, the complex dielectric constant $\tilde{\epsilon} = \epsilon_1 + i\epsilon_2$

$$\epsilon_1 := 1 + \chi_e$$

The Drude-Lorentz model express the polarizability χ_e as:

$$\chi_e = \frac{Ne^2}{\epsilon_{vac} m_e} \cdot \left(\frac{1}{\omega_0^2 - \omega(\omega + i\gamma_j)} \right)$$

With N the number of electrons of charge e and mass m_e contributing to the polarization of

2. EXPERIMENTAL METHODS

the material. The "spring constant" forces the moving charges to return to their initial position in such a way that they resonate at a frequency ω_0. ϵ_{vac} being the dielectric constant of vacuum. In the quantum mechanical framework, ω_0 is the transition frequency of an electron between two energy levels separated by $\hbar\omega_0$. For simplicity we assumed two discrete energy levels however, in actual samples, all energy levels are smeared out and it is more appropriate to write the former equation as:

$$\chi_e = \frac{Ne^2}{\epsilon_0 m_e} \cdot \sum_j \left(\frac{f_j}{\omega_{0j}^2 - \omega(\omega + i\gamma_j)} \right) \tag{2.1}$$

This equation sums up the contribution of all possible transitions j, each with frequency ω_{0j} and transition strength f_j. The oscillator strengths f_j satisfy the requirement (oscillator strength sum-rule) $\sum_j f_j = 1$ which measure the relative probability of a quantum mechanical transition.

A graphical representation of the frequency dependence of ϵ is provided in Figure 2.1. As the frequency approaches the resonance frequency ω_0, ϵ_1 diverges (Figure 2.1 a)). Γ represents the damping of an oscillator, its quantum-mechanical counter-part being energy dissipation in the form of a decay process.

Polarization involves different mechanisms throughout the spectrum. At high frequencies, no charge can follow the electric field oscillation and the dielectric constant resumes to that of vacuum. The resonant oscillation for electric polarization occurs in the UV/Vis and in the infrared region for vibrational polarization. When the frequency approaches 0, the value of ϵ_1 is represented by the static dielectric constant ϵ_s. Equation 2.1 tells us that this value includes the contribution of all frequency oscillations.

While ϵ_1 is proportional to the electric permittivity, ϵ_2 is proportional to light absorption in the material. As explained earlier, the electric permittivity is due to the coupling (resonant interaction) of light with polarization modes. For this reason, any contribution to ϵ_1 is concomitant with a peak in ϵ_2 as shown in Figure 2.1c.

The simplest form of light propagation regards a traveling wave $\phi = A \cdot cos(Kx - \omega t))$, with $K = 2\pi/\lambda$ the wave number and $\omega = 2\pi\nu$ the angular frequency. This expression represents a wave with a periodicity in space (x) and time (t). The following equation is used to express the propagation of the electric and magnetic component of light:

$$E = E_0 \cdot cos(Kx - \omega t)$$
$$B = B_0 \cdot sin(Kx - \omega t)$$

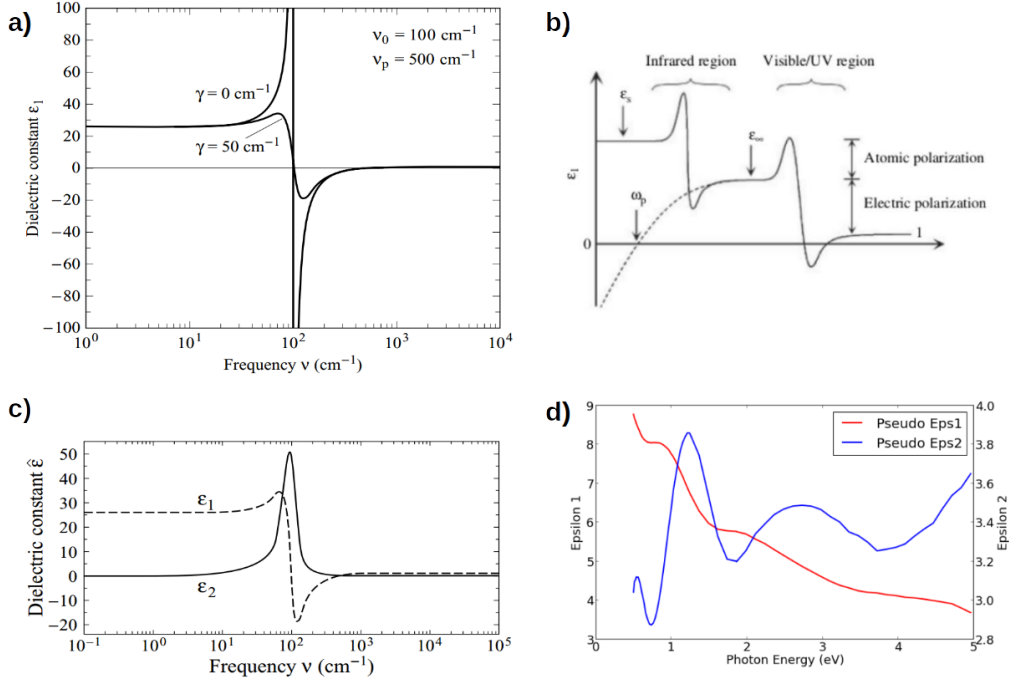Light propagates through space and time as a periodic perturbation of the electro-magnetic

Figure 2.1: Figure from M. Dressel and G. Grüner [12] a) Real part of the dielectric function with ($\gamma \neq 0$) and without ($\gamma = 0$) energy dissipation as a function of wavenumber. b) Different contributions to the overall dielectric constant spectrum. c) Real and imaginary part of the complex dielectric constant as described by the Drude-Lorentz model. d) Real and imaginary part of the complex dielectric constant of a real sample.

field (Figure 2.2). While the electric field vector **E** interacts with the electric dipole moments, the magnetic field vector **B** interacts with magnetic moment. Maxwells' law of induction states that electric field variation is always concomitant to a magnetic field variation.

As ϵ of the material is not equal to ϵ_{vac}, the speed of light inside the material (v) is not the same as the speed of light in vacuum (c). The ratio of these two quantities is the refractive index $n := c/v$, thus we have:

$$K = \frac{\omega n}{c} = \frac{2\pi}{\lambda}$$

We can then write the amplitude of the light electric field as:

$$E = E_0 \cdot cos\left(\frac{\omega n}{c}x - \omega t\right) \tag{2.2}$$

using the Euler identity, we can rewrite the oscillation of the electric field as:
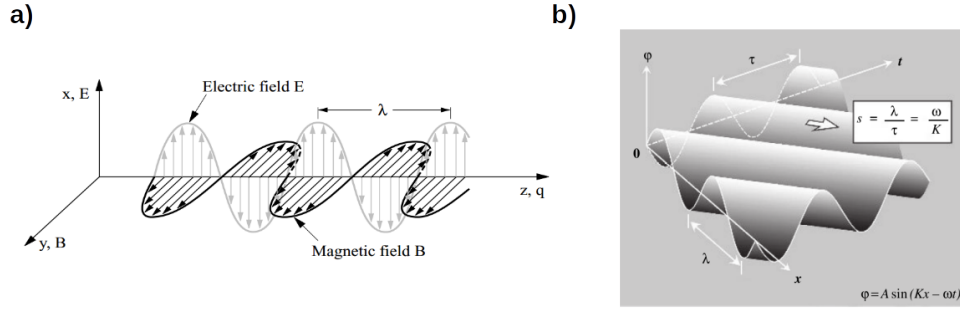
Figure 2.2: Figure from M. Dressel and G. Grüner [12] a) Electric and magnetic field of a periodic electro-magnetic field perturbation. Figure from H. Fujiwara [13] b) Space and time evolution of the electric field of light

$$\tilde{E} = E_0 \cdot exp\left[i\left(\omega t - \frac{\omega n}{c}x\right)\right]$$

Substituting n with its complex representation $\tilde{n} = n - ik$ gives:

$$\tilde{E} = E_0 \cdot exp\left[i\left(\omega t - \frac{\omega \tilde{n}}{c}x\right)\right]$$
$$= E_0 \cdot exp\left(-\frac{\omega k}{c}x\right)exp\left[i\left(\omega t - \frac{\omega n}{c}x\right)\right]$$

The electric field amplitude now has a damping term $(-\frac{\omega k}{c}x)$ that accounts for the extinction of light traveling into a medium. The wavelength of light then becomes $\frac{2\pi c}{\omega n}$ and accounts for the propagation velocity change. The refractive index has a clear physical meaning: the real part causes the light to change its frequency when traveling into a material as shown in Figure 2.3a. The imaginary part k of the refractive index measures the amount of light absorbed by the material (Figure 2.3b). This gives the expression of an electromagnetic wave propagating through an absorbing medium in terms of physical observables.

2.2 Spectroscopic ellipsometry

Spectroscopic ellipsometry is an optical measurement technique relying on the change of polarization state of light upon reflection or transmission onto a sample [13]. The term "ellipsometry" originates from the fact that, most of the time, light polarization becomes "elliptical" following interaction with the sample. In this chapter, I explain how light interacts
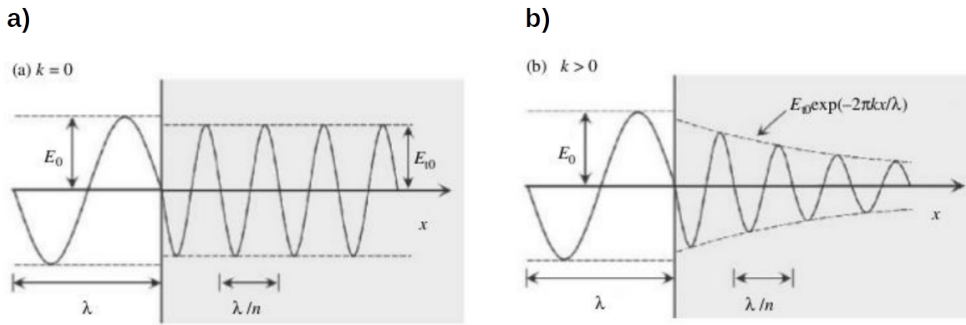
Figure 2.3: Figure from H. Fujiwara [13]. Representation of an electro-magnetic wave propagating into a transparent medium (a) and light-absorbing medium (b)

with matter and how it is changed upon reflection and refraction. This knowledge allows obtaining the dielectric constant of a material. One great advantage of spectroscopic ellipsometry is that it gives access to both the real and imaginary parts of the dielectric constant. Other spectroscopic techniques such as transmission or reflection require assumptions regarding the parts of the spectrum outside the measured range in order to perform a Kramers-Kronig transformation. Numerical extrapolations must be conducted outside the measured frequency range which may influence the final result. Moreover, ellipsometry does not require any reference measurement and thus the method is, so to speak, "self-calibrated". Ellipsometry is precise, quick and well suited for film characterization.

2.2.1 Fresnel Coefficients

The Fresnel reflection coefficient $\tilde{r}$ expresses the ratio between reflected and incident electric fields, $\tilde{E}_r$ and $\tilde{E}_i$ respectively. Because the response of the material to incident light differs from one material to another, this ratio is a complex number that can be written in terms of the ratio of the reflected and incident electric field magnitudes as well as their relative phase. This provides a convenient method of separately handling these two quantities. This gives:

$$\tilde{r} = \frac{\tilde{E}_r}{\tilde{E}_i} = |\tilde{r}|e^{i\phi}$$

The orientation of the electric field vector, or in other words the light polarization state, can be written in terms of two orthogonal components: the s- and p- polarized light. They are respectively perpendicular and parallel to the plan of incidence. When crossing an interface between two materials with different refractive index, these two components behave differently upon reflection. This gives:

$$\tilde{r}^s = \frac{\tilde{E}_r^s}{\tilde{E}_i^s} = |\tilde{r}^s|e^{i\phi^s} \qquad \tilde{r}^p = \frac{\tilde{E}_r^p}{\tilde{E}_i^p} = |\tilde{r}^p|e^{i\phi^p}$$
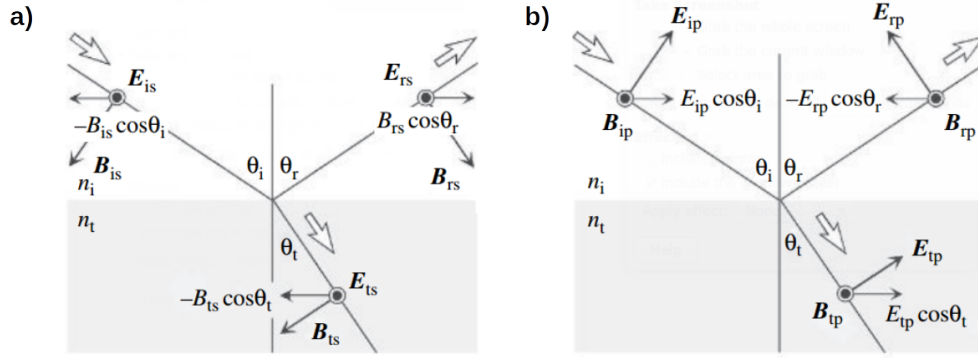

Figure 2.4: Figure from H. Fujiwara [13]. Detail of the tangential and normal components of the electric field vector for s- and p- polarized light.

Figure 2.5 a) shows the Fresnel coefficient as a function of the incident angle. For a purely refractive medium $\tilde{r}^p$ and $\tilde{r}^s$ are real numbers. While r^s is always negative, r^p becomes negative for angles of incidence larger than the Brewster angle. The sign of the coefficient is determined from the phase variation that occurs when light is reflected and refracted at an interface. The ratio between reflected and incident electric field amplitudes being negative represents a phase shift of 180 degree, while this ratio being positive represents no phase shift. This is represented by a step function as shown in Figure 2.5 b). This phase shift is a consequence of the Maxwell equations which require that the electric field $\tilde{E}$ must be continuous across the interface. Referring to Figure 2.4, we can write:

$$E_i^p \cos\theta_i - E_r^p \cos\theta_r = E_t^p \cos\theta_t$$
$$E_i^s + E_r^s = E_t^s$$

On the incidence side there are both the incident and reflected field and their sum must have the same phase as the transmitted wave regarding the continuity conditions. Writing down the boundary conditions for tangential and normal components (more details in Appendix A.1), we find that the only way that continuity can be upheld is to have the incident and transmitted waves in phase, while the reflected wave may be either exactly in or out of phase, depending on whether the waves are crossing an increase or decrease in refractive index.

When light is reflected off the sample, $\tilde{r}^s$ and $\tilde{r}^p$ are superimposed. What ellipsometry
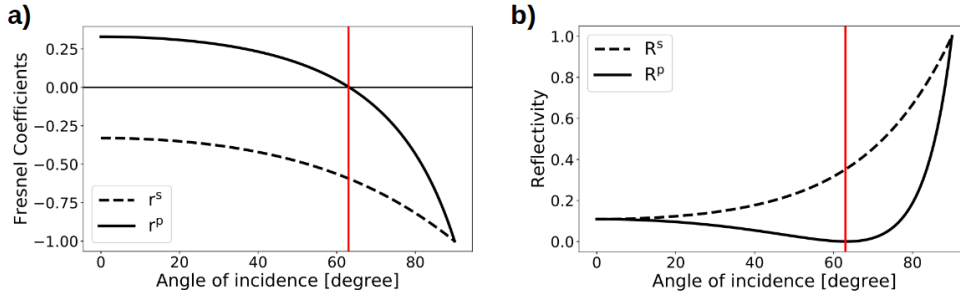
Figure 2.5: Incident angle dependence of the Fresnel coefficients a) and the s- and p-reflectivities b) In b) R^s and R^p are identical at normal incidence because there is no way to distinguish the two polarizations in this configuration. The Brewster angle is at the vertical line.

actually measures is the ratio $\frac{\tilde{r}^p}{\tilde{r}^s}$. Due to difference in the electrical dipole radiation, p- and s-polarization show different changes in amplitude and phase. This ratio is written as:

$$\tilde{\rho} \; = \; \frac{\tilde{r}^p}{\tilde{r}^s} \; = \; \frac{tg\,\Psi^p}{tg\,\Psi^s}e^{i(\Delta^p-\Delta^s)} \; = \; tg\Psi e^{i\Delta}$$

$tg\Psi$ represents the amplitude ratio between reflected p- and s-polarization while Δ expressing the phase difference between reflected p- and s-polarization.

2.2.2 Principles of ellipsometry

An ellipsometer measures two values Ψ and Δ by using polarized incoming light and analyzing its state of polarization. Several methods exist, such as nulling ellipsometry or phase-modulated ellipsometry. In this work, we used a rotating analyzer ellipsometer (RAE) [13].

The typical configuration for RAE is as follow:

$$\text{Source} \rightarrow \text{Polarizer} \rightarrow \textbf{Sample} \rightarrow \text{Analyzer} \rightarrow \text{Detector}$$

The light emitted by the source is oriented towards a grating which resolves the beam into monochromatic light. This monochromated light is linearly polarized by the first (fixed) polarizer. The electric field component of the light can always be decomposed into two orthogonal contributions: one in the plane of incidence (E_p^i) and another perpendicular to it (E_s^i). Before hitting the sample, the linearly polarized light has these two components in phases. The sample will reflect these two components not only with a different intensity, but also with a different phase (even if the sample itself is optically isotropic) which causes the reflected light to become elliptically polarized. Ellipsometry consists of measuring the degree of ellipticity of the light

15

reflected off the sample as a function of analyzer angle A [14]. This is done by probing the intensity of light in all possible directions of polarization. The analyzer, (a rotating polarizer), modulates the light intensity into a signal that has the form:

$$\frac{I(A)}{\langle I(A) \rangle} = 1 + \alpha cos(2A) + \beta sin(2A)$$

with α and β the Fourier coefficients of the signal. We then have

$$\alpha = \frac{tan^2\Psi - tan^2P}{tan^2\Psi + tan^2P} \qquad \beta = \frac{2tan\Psi cos|\Delta|tanP}{tan^2\Psi + tan^2P}$$

with P the input polarizer azimuth with respect to the plane of incidence. The shape of $I(A)$ shifts in the horizontal direction (analyzer angle) as Ψ is varied. On the other hand, the amplitude of $I(A)$ reduces as the state of polarization changes from linear to elliptical. We can see that the polarization state of the reflected light in RAE is determined by the variation of light intensity with the change of the analyzer angle.

Solving the above equation for Ψ and $|\Delta|$ gives:

$$tan\Psi = \sqrt{\frac{1+\alpha}{1-\alpha}}tanP \qquad cos|\Delta| = \frac{tanP}{tan\gamma}\frac{\beta}{1-\alpha}$$

The two parameters α and β are first determined by Fourier analysis of the measured reflected light intensity. We then used the above equations to calculate Ψ and $|\Delta|$. Note that additional information is required to obtain the sign of Δ.

2.3   Measuring with an Ellipsometer

2.3.1   Brewster Angle

When light meets an interface at an incident angle $\Theta_i \neq 0$, light is transmitted into the medium. The electric field resonates with the electric dipole of the material. The angle at which light is refracted is given by Snell's law. S- and p- polarized light behave differently at the interface. When p-polarized light propagates through a medium, the polarization remains within the plane of incidence, perpendicular to the direction of propagation as shown in Figure 2.6. As the incident angle increases from 0° (normal incidence) to 90° (grazing incidence), the light beam meets an angle at which the polarization of the medium oscillates in the same direction as the reflected light. Because the electric field is always perpendicular to the direction of propagation in this configuration, the angle between reflected and refracted light would be 90°. However no light can be radiated parallel to the direction of oscillation. For this reason, at
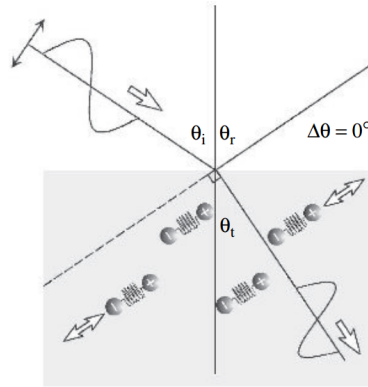
Figure 2.6: Figure from H. Fujiwara [13]. Incoming p-polarized light at the Brewster angle. Refracted light propagates perpendicularly to the direction of the virtually reflected light. The electric dipole oscillates perpendicular to the refracted light. Because no energy radiates in a direction parallel to a charge oscillation, the reflected p-polarized light is suppressed

this particular incident angle, no p-polarized light is reflected. This angle is called the Brewster angle. As shown in Figure 2.5 b), the reflectivity R^p goes from a non-zero value at $\theta_i = 0$ to 0 at $\theta_i = \theta_{Brewster}$. For incident angles larger than θ_B, it rises again to 1 at normal incidence. S-polarized light behaves quite differently as indeed, no matter the value of the incident angle, the polarization will always be perpendicular to the reflected beam. For this reason, R^s increases gradually with an increasing incident angle. Thus, at the Brewster angle only s-polarized light is reflected. This is why this angle is also called the polarization angle.

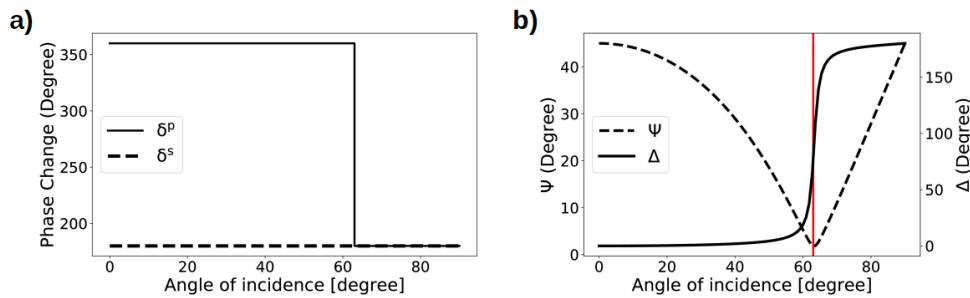**Figure 2.7:** Phase change of the s- and p-polarized light upon reflection off the sample a) Incident angle dependence of Ψ and Δ. The Brewster angle is at the vertical line.

2.3.2 Optimal Angle Determination

In order to maximize the signal intensity observed by the detector, light must be as circularly polarized as possible. This occurs at the Brewster angle, the angle at which reflected light

is perfectly s-polarized. As shown in Figure 2.7 b), at this angle, Δ goes from 180 (linearly polarized light) to 0 (no phase difference as one polarization drops to zero). The value of Δ does not follow a step-like function because, in reality, the material is absorbing. Instead, the transition from 180 to 0 is smoothed and Δ goes through the value of 90 degrees. The signal from the detector will thus be optimal at the Brewster angle since the light is circularly polarized. For this reason, we measure at a Δ as close to 90 degrees as possible. Since the reflected light is constituted by at least two reflections (thin film and substrate), we talk about a pseudo-Brewster angle. The value of this angle depends on the effective refractive index of the system (film + substrate) and is thus highly material as well as frequency dependent. Usually, the higher the refractive index, the higher the Brewster angle. With our fixed angle ellipsometer, it is thus impossible to optimally measure across the whole spectrum. Moreover, as we cross the MIT, the refractive index of our sample changed significantly, which complicated measuring the temperature-dependent dielectric constant spectrum. We made it possible at a fixed angle at the cost of some singularities in the spectra that we corrected afterwards. This issue is addressed in detail by the numerical method below.

2.4   Temperature cycle

In order to achieve greater insight into the electronic structure as we pass through the phase transitions (IMT and MPT), we need a temperature-dependent evolution of the dielectric constant of the material. To this end, we cooled our sample to 50° K inside a homemade cryostat using liquid helium as a cryogenic liquid. In order to avoid condensation of air components on the surface of the sample, we set a vacuum of 10^{-8} mbar by first using a primary pump to reach to 10^{-2} mbar. We then used a turbo-pump to reach 10^{-7} mbar and finally an ionic pump to reach 10^{-8} mbar. Once a sufficient vacuum was achieved, we began to cool down. In order to attain high temperature resolution, we ensured the cooling process was sufficiently slow for one spectrum to be taken every single Kelvin. To accomplish this, we used a valve that regulates helium flow in combination with a heater near the sample. Such an installation grants full control over the speed at which the sample is cooled down. This allows achieving the required resolution and a precise insight of the sample's behavior at the transition temperature. Additional precaution is taken to ensure cooling and warming occurs at fixed and constant rates.

   Because ellipsometry is highly sensitive to surface morphology as well as incident angles, we want to minimize the deviation from the initial position due to contraction of the sample holder. Our homemade cryostat is designed in such a way that the sample is suspended to the piece in contact with the cold finger by a collection of thin copper wires as shown in Figure 2.8. In this way, linear contraction due to cooling is minimized and the light beam always hits the

sample at the same position.
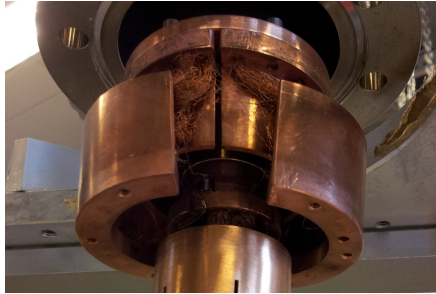
Figure 2.8: Heat bridge comprised of copper wire providing minimum contraction the during cool down process
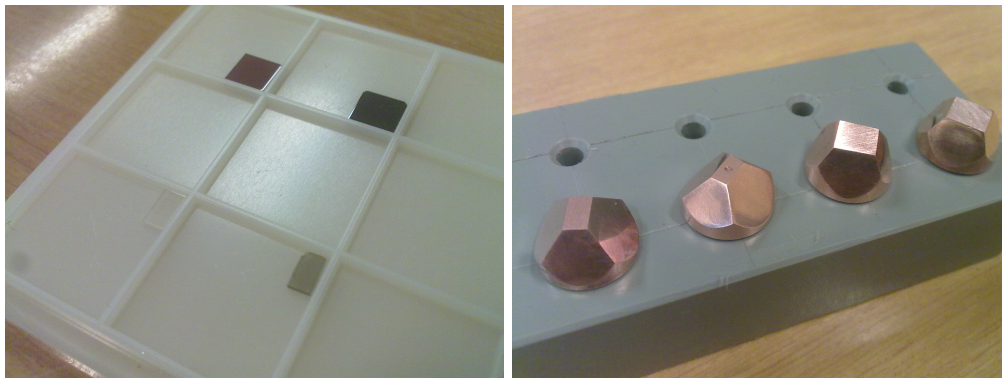
Figure 2.9: a) Details of the substrates as well as their film-covered counterparts. On the left, are the two different substrates: up) NGO down) LAO. On the right: up) NNO/NGO down) SNO/LAO. Both ultra-thin films already show noticeable absorption in the visible range. Surface is as free of imperfection as it can be. b) The sample holder is designed to position the surface of the film at the focal point of incident light. The edges are designed so that any light falling around the sample will not be reflected toward the detector. Samples are glued with silver paste in order to guarantee adequate heat contact.

2. EXPERIMENTAL METHODS

Numerical methods

In this section, the numerical tools used to process the raw measured data are presented.

3.1 Fresnel Equations

We explain the derivation of Fresnel equations for the system under study: involving a three-layer model with two semi-infinite layers (air and substrate) and one thin film. Such a system consists of two interfaces. Light is reflected at each interface so the total reflected light is the superposition of several beams. Fresnel equations consist of a set of relations that relate the intensity of the reflected light beam with the incident angle and the refractive indexes of the different mediums.

In order to describe these relationships we begin with the representation of the two orthogonal polarizations of light: the s- and p-polarizations. The s-polarization (from the German senkrecht meaning perpendicular) is perpendicular to the plane of incidence while p-polarized light is parallel to the plane of incidence. Any light polarization state can be described in terms of these two perpendicular polarization states. Figure 3.1 shows the electric field vector of the p-polarized light before and after reflection. The reflected light r is by definition the ratio between the reflected electric field E_r and the incident electric field E_i intensities. For the two perpendicular s- and p- polarizations of light we have:

$$r^s = \frac{E_r^s}{E_i^s} \qquad r^p = \frac{E_r^p}{E_i^p}$$

The amplitudes of reflected light r^s and r^p are called the Fresnel coefficients. In general, the phase-shift imprinted to the light at the interface requires the use of complex electric field $\tilde{E}$. In such situation, reflectivities are complex values ($\tilde{r}$). Writing down the constraints imposed by
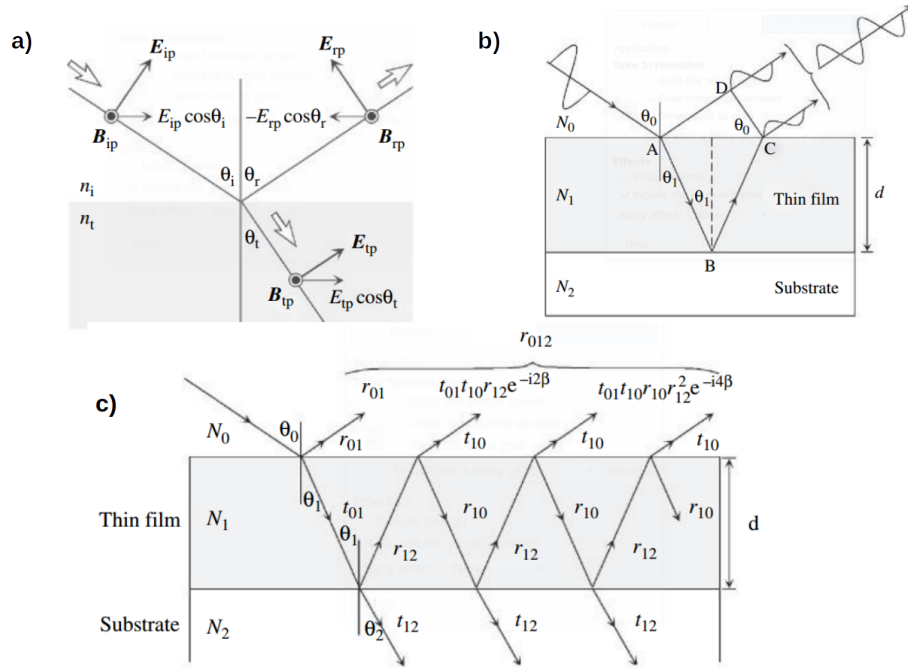
3. NUMERICAL METHODS

Figure 3.1: Figure from H. Fujiwara [13]. This represents the model for Fresnel equations. c) The total light reflected off the sample is given by the sum of the light reflected at each interface. r_{ij} and t_{ij} represent amplitudes of reflected and transmitted light respectively.

the boundary conditions we have: (see Appendix A.1)

$$\tilde{r}^p = \frac{\tilde{N}_t \cos\theta_i - \tilde{N}_i \cos\theta_t}{\tilde{N}_t \cos\theta_i + \tilde{N}_i \cos\theta_t} \qquad \tilde{r}^s = \frac{\tilde{N}_i \cos\theta_i - \tilde{N}_t \cos\theta_t}{\tilde{N}_i \cos\theta_i + \tilde{N}_t \cos\theta_t} \qquad (3.1)$$

with i and t the index of the optical path, namely the incident or transmitted light, respectively. $\tilde{N} := n + ik$ is the complex refractive index of the material and θ the angle between the light beam and the line perpendicular to the surface at the reflection point.

For systems with more than one interface, Figure 3.1c shows how multiple reflections adds up to form the resulting overall reflection. Of course, interferences occur in such configuration and for this reason, we are interested in knowing the phase shift between the primarily reflected beam and all other beams reflected from the interface below. Figure 3.1b shows the optical path difference between two consecutive beams traveling toward the medium of incident light. We define the film phase thickness as β. The phase difference 2β is proportional to the optical path difference of the two beams. The quantity 2β represents the phase difference acquired by the light by traveling twice through the film: once transmitted from the incident light, and once again from the interface below. This process, represented in Figure 3.1c, occurs repeatedly. At each iteration of this process, the light acquires a phase shift 2β. We then have (see Appendix

A.3)

$$\beta = \frac{2\pi d n_1}{\lambda} \cdot cos\theta_1 \tag{3.2}$$

The phase of the light electric field after traveling twice through the film is then $e^{-2i\beta}$. This allows us to sum the contribution of all beams as the total reflectivity $\tilde{r}_{012}$. There is virtually an infinite numbers of beams that contribute to the total reflectivity. The sum of all these terms forms an infinite series that resumes to a simple fraction (see Appendix A.4)

$$\tilde{r}_{012}^s = \frac{r_{01}^s + r_{12}^s e^{-2i\beta}}{1 + r_{01}^s r_{12}^s e^{-2i\beta}} \qquad \tilde{r}_{012}^p = \frac{r_{01}^p + r_{12}^p e^{-2i\beta}}{1 + \tilde{r}_{01}^p r_{12}^p e^{-2i\beta}} \tag{3.3}$$

were 0,1 and 2 are indexes that indicate the medium where the beam is considered. Regarding Equations 3.1, index i and t (incident and transmitted beams) would be 0 and 1 respectively. At this point, we have everything required to calculate the complex refractive index of the film. As can be seen from Equation 3.1, 3.2 and 3.3, however, it is impossible to write $\tilde{N}_1$ as a function of $\tilde{r}_{012}$ in analytically closed form. Thus $\tilde{N}_1$ must be determined numerically. The algorithm is as follow: we first compute $\tilde{r}_{012}$ by guessing $\tilde{N}_1$ and then varying this quantity until we reproduce $\tilde{r}_{012}$ that was measured with the ellipsometer. The numerical process used to solve this inverse problem is discussed below. This algorithm is represented graphically in Figure 3.2

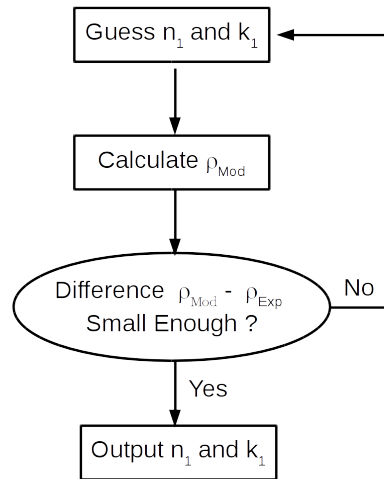**Figure 3.2:** First we calculate $\tilde{\rho}_{Mod}$ from mathematical models with initial n_1 and k_1. The real and imaginary parts of $\tilde{\rho}_{Mod}$ are compared to the real and imaginary part of $\tilde{\rho}_{Exp}$. The two differences are minimized to a given threshold. That is χ^2 is minimized in the least square sense. At this stage, provided the model is correct, we have the value of n_1 and k_1

3.2 Inversion of measured data

In this subsection, I explain the implementation of the mathematical model discussed above as well as how to calculate $N_1 = n_1 + ik_1$ backwards from Ψ and Δ. Full details of the code can be found in Appendix A.5. I also show how an inverse problem can be addressed using iterative process.

Using the Python programming language version 2.7, we write down functions that compute the different reflectivities as well as β

```python
def r1s(n1,k1):
    a = n0*np.cos(phi0)
    b = (n1+k1*1j)*np.cos(phi1(n1))
    Reflect1s = (a - b) / (a + b)
    return Reflect1s
...

def delt1(n1,k1):
    delta1 = 2*np.pi*(n1+k1*1j)*thick1*np.cos(phi1(n1))/wl
    return -delta1

def ReflectS(n1,k1):
    Rs = (r1s(n1,k1) + r2s(n1,k1)*np.exp(-2*1j*delt1(n1,k1))) \\
        / (1 + r1s(n1,k1)*r2s(n1,k1)*np.exp(-2*1j*delt1(n1,k1)))
    return Rs
...

def CalcRho(n1,k1):
    rho = ReflectP(n1,k1) / ReflectS(n1,k1)
    return rho
```

We then evaluate rho (ρ) calculated using the above Fresnel equations (ρ_{Exp}) with respect to the rho provided by the measured ellipsometric data $\rho_{Exp} = \frac{R_s}{R_p} = tg\Psi e^{i\Delta}$. We minimize the differences between these two values by varying the value of $\tilde{N}_1$. As we handle complex numbers, we must minimize both the real and the imaginary parts differences. This is accomplished by writing an "objective function" that returns a single value (χ^2) that accounts for the differences between the two numbers:

```python
def Fit_n1(Initn1):
    In1 = Initn1['n1'].value
    diff =  CalcRho(In1,k1) - ExpRho
    return diff.real**2 + diff.imag**2

def Fit_k1(Initk1):
    Ik1 = Initk1['k1'].value
```

```
    diff =  CalcRho(n1,Ik1) - ExpRho
    return diff.real**2 + diff.imag**2
```

n_1 and k_1 are fitted sequentially because minimization algorithms usually deal with a set of parameters rather than complex numbers explicitly. The many variables that enter a model may be constrained. For a complex number, the Kramers-Kronig relationship relate their real and imaginary parts. In this code, I did not use such constraints and my data are thus Kramers-Kronig inconsistent. The reason of doing this is that the ellipsometry measurements themselves may deviate from Kramers-Kronig consistency due to experimental signal noise. Thus the algorithm would not successfully fit KK-consistent variables to KK-inconsistent data.

Using least-square minimization routines (the "minimize" method from Minimizer object) as implemented in Lmfit [15], we instantiate a Minimizer object by providing the above-mentioned objective function plus an initial guess for n_1 and k_1. The minimize method will then return the fitted value of the parameters n_1 and k_1 together with the χ^2 value.

```
for l in range(NbrIter):

        CC = Minimizer(Fit_k1,Param_k1,nan_policy='omit')
        DD = CC.minimize(method=MinMethod)

        k1 = DD.params['k1'].value
        Set_k1(k1)

        AA = Minimizer(Fit_n1,Param_n1,nan_policy='omit')
        BB = AA.minimize(method=MinMethod)

        n1 = BB.params['n1'].value
        Set_n1(n1)

        Alln1[i] = BB.params['n1'].value
        Allk1[i] = DD.params['k1'].value)
```

The problem to be solved here at each point of the spectrum, is a problem with two unknowns (n_1 and k_1) for two measured variables (Ψ and Δ). While being fully determined, this problem is not uniquely defined. Indeed, $\tilde{\rho}_{calc}$ cannot be written in terms of n_1 and k_1 since it is a functional of $R^p(n_1, k_1)$ and $R^s(n_1, k_1)$. Due to the presence of several local minima, direct data inversion (unambiguous analytical solution) is impossible and the minimization algorithm is likely to converge to a wrong solution. This problem was addressed by Gilliot who proposed to draw a map of all available solutions and choose the physically relevant one [16]. In our lab, using Reffit, we managed to isolate two of the many available solutions. Since one was unphysical (wrong sign of $Im(\tilde{\epsilon})$), we were left with a unique solution.

Figure 3.3 shows how well the fit converged. Also, it shows a comparison between two different methods used in our lab. The one described here and the other one implemented in Reffit.

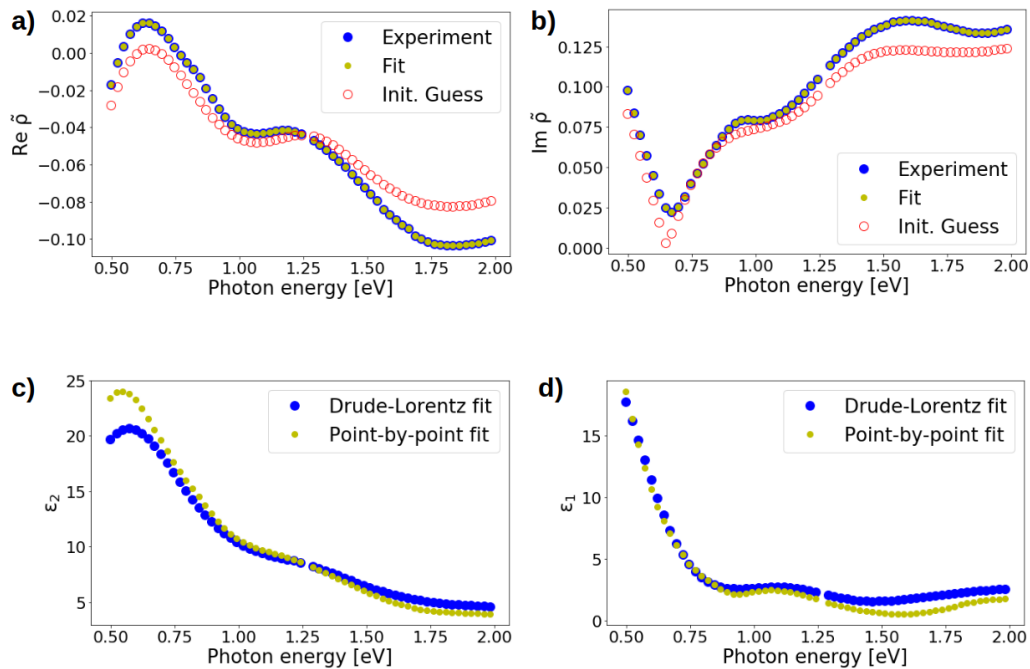**Figure 3.3:** Top: Real (a) and imaginary (b) part of $\rho(\omega)$ at 80° K. The initial guess is the pseudo-dielectric function calculated directly from the ellipsometric measurements of the film+substrate. The fit was tested against several initial guess and is quite robust. Bottom: comparison between epsilon inverted using the above method (point-by-point fit) and using a Drude-Lorentz fit (reffit)

Chapter 4

Theoretical Models of the RE nickelates

4.1 Electronic Correlation

The many-body physics of interacting electrons is key to the understanding of any material properties such as color, transparency, heat and electric conductivity. Every property of a material can be understood knowing its electronic structure and dynamics. Many properties such as resistivity or light absorption can be understood in terms of independent particle dynamics. The physics of independent electrons describes single electrons traveling in a static potential, meaning without dynamic interaction with other electrons and/or lattice vibrations. In solid state physics, this is known as "band theory" and has been successfully used to understand simple solids such as copper and silver.

Most materials however cannot be understood in terms of single particle physics, copper oxide CuO being one example. Density functional theory predicts a 0.3 eV gap in NiO resulting from anti-ferromagnetic order [17], whereas cluster calculations accounting for the Coulomb interactions arrive at a gap of 5 eV [18]. The gap was experimentally found to be 4.3 eV [1]. Many other materials such as transition metal oxides violate the expectation of the band theory. Such materials, which are supposed to be metallic according to band theory but are actually insulators, are called "Mott insulators". They represent a class of materials where the interaction between electrons plays a central role. Such materials cannot be understood in terms of single electron dynamics. Indeed, due to electronic correlation the electrons are coupled and give rise to several many-body states. Electronic correlation is strongest in d and f shells as these shells are deeply confined inside the atom.

Mott was the first to formulate the idea that electronic correlation may be due to the Coulomb interaction [19]. From this idea, Hubbard showed that sufficiently strong on-site Coulomb repulsion can localize electrons [20]. A gap that opens due to a Coulomb interaction is called a Mott gap.

Figure 4.1 shows a schematic representation of the electronic structure of a Mott insulator.
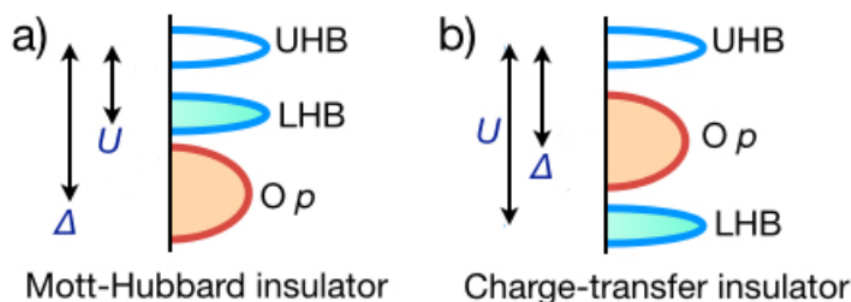
Figure 4.1: Figure from S. Ciuchi [21]. Density of states of a Mott insulator a) and a Charge Transfer Insulator b). The Coulomb interaction U splits the band into a Upper Hubbard Band (UHB) and a Lower Hubbard Band (LHB), where the bandwidth W is proportional to the inter-atomic hopping. The distance between the two bands is proportional to the magnitude of U.

O2p states are represented because of possible hopping process between O2p and TM d states. Within this picture, an additional energy scale, Δ, is needed to represents the energy required to transfer an electron from an O2p level to a TM 3d level. Figure 4.1 a) shows the situation where $U < \Delta$. In this situation, because the two Hubbard bands are well separated, the band gap energy in such systems is mainly controlled by U. On the other hand, we can have the situation $\Delta > U$ (b). In this situation, the oxygen level takes place within the Mott gap and the gap energy is measured between the top of the O2p level and the bottom of the UHB. Such systems are called charge transfer insulators because the lowest energy excitation involves the transfer of an electron from an O2p orbital to an TM 3d orbital. In these materials, the band gap is then mainly controlled by the amplitude of Δ. In this context, we would expect that a sufficiently small charge transfer gap, Δ, would progressively lead to a metallic behavior. What occurs in reality is the opening of a gap due to the hybridization of the ligand p states and the transition metal (TM) 3d states. For small to negative charge transfer, these states are indeed very close in energy, allowing the formation of bonding and antibonding states as predicted by the molecular orbital theory. Hybridization separates the states of similar energy in order for the electrons to coexist, thus forming an energy gap. Such a gap leads to a so-called covalent insulating regime [22] also referred to in literature as a negative charge transfer insulator [23]. The charge transfer energy is the energy required to create a ligand hole $\underline{L}$. When this energy is negative, hole creation is energetically favorable and spontaneous.

4.2   Rare-Earth Nickelates

According to the Zaanen-Sawatzky-Allen (ZSA) scheme [24], nickelates enter the class of negative charge transfer insulators and are thus discussed within this context. The electronic

configuration of nickel in nickelates is formally $3d^7$ but the hybridization of the Ni d orbital with the ligand hole creates other states such as $3d^8\underline{L}$ or $3d^9\underline{L}^2$. The ground state of nickelate can then be written as a superposition of all these states:

$$|GS\rangle = \alpha \left|d^7\right\rangle + \beta \left|3d^8\underline{L}\right\rangle + \gamma \left|3d^9\underline{L}^2\right\rangle$$

Calculations show that β is the largest coefficient [25]. We then assume from now on that the ground state of nickelates is essentially a $3d^8\underline{L}$ state. Important here is the existence of a hybridized hole state. Such a state may be delocalized over the whole network and will be used to explain an ambiguity in nickelates regarding the presence of bond-disproportionation without charge-ordering.

Synchrotron X-ray diffraction (SXRD) of $YNiO_3$ [26], neutron diffraction [27, 28] as well as Mössbauer spectroscopy [29] show evidence of two different Ni-O bond lengths in the insulating phase. Crystallographic evidences also exist for bond-disproportionation in all nickelates in the insulating phase [30–33] which indicate a common feature for this class of material. The insulating phase is characterized by two sublattices. In one of them, the Ni-O bond-length is decreased compared to the metallic state. In the second, this bond-length is increased, effectively forming a bond-disproportionated state.

Charge-ordering has been discussed extensively to explain the presence of inequivalent bond-lengths within the same crystal [30, 34, 35]. Charge-order has also been invoked to explain the highly unusual AFM structure of the insulating phase. Several experiments suggest that there are two different types of nickel electronic configurations [10, 36]. A complete charge-disproportionation of the type $2Ni^{3+} \rightarrow Ni^{2+} + Ni^{4+}$ has been proposed. Such a configuration would create a magnetic $d^8_{S=1}$ as well as a non-magnetic $d^6_{S=0}$ state. The magnetic states would couple antiferromagnetically, effectively doubling the unit cell of the magnetic phase. This magnetic phase thus involves 4 unit-cells and gives rise to the propagation vector $\mathbf{k} = (1/2, 0, 1/2)$ which is common to the whole family of nickelate compounds [10, 36, 37].

Despite being so likely, the experimental evidence so far that confirms the existence of a charge-order is indirect. Moreover, the exact state is difficult to define. Actually, such a charge configuration would involve electron transfer from one nickel site to another, but is expected to be forbidden because of the large Coulomb repulsion acting within the nickel 3d shell. Recent X-ray diffraction seems to confirm this assumption [38].

An alternative view has emerged however, involving an inhomogeneous hole distribution over the crystal. Sawatzky et al. first conducted Hartree-Fock calculations [39] on 3d TM oxides with small to negative Δ. They showed that ligand holes, just like nickel sites, may undergo a charge order. They proposed that one oxygen site over two may have more holes than the other half. This excess of holes causes FM coupling between two Ni sites, explaining the up-up-down-down spin stacking. In this picture, the spin ordering at the metal site couples

with the charge order at the oxygen site without explicit doping or any orbital ordering.

Similar to this picture is the idea of inhomogeneous hole distribution around Ni sites termed by Marianneti et al. as site-selective Mott insulators [40]. Each nickel sublattice is surrounded by a different hole density. In the extreme limit of this picture, the nickel 3d electron of one sublattice forms a long-bond (LB) and is completely decoupled from the surrounding nickel, while the d electron of the second sublattice forms a short-bond (SB) which is strongly coupled between each other. The DMFT calculation showed that each site has a high-spin $3d^8$ electronic configuration. On the LB site (Ni_1), this results in a local moment while on the SB site (Ni_2), the coupling to the two oxygen holes lead to a singlet state.

The insulating phase of nickelates shows a characteristic two-peak structure in the near-infrared part of the spectrum [41]. The nature of these two optical transitions is explained in detail in the next chapter. We showed that the insulating phase of nickelate is a mixed, Peierls-Mott phase. In such a phase, the long range partial charge order (breathing distortion) opens a Peierls gap (in the energy range 0.5-0.7 eV) above the Fermi energy. The insulating nature of the nickelate originates from the Coulomb repulsion U and the Hund's coupling J acting within the e_g state. A Mott gap opens provided the effective Coulomb energy U-3J is smaller than the energy difference between the two different nickel sites. The two transitions observed in the insulating phase come from transitions across the Peierls gap and across the Mott gap as described in more detail in [42]

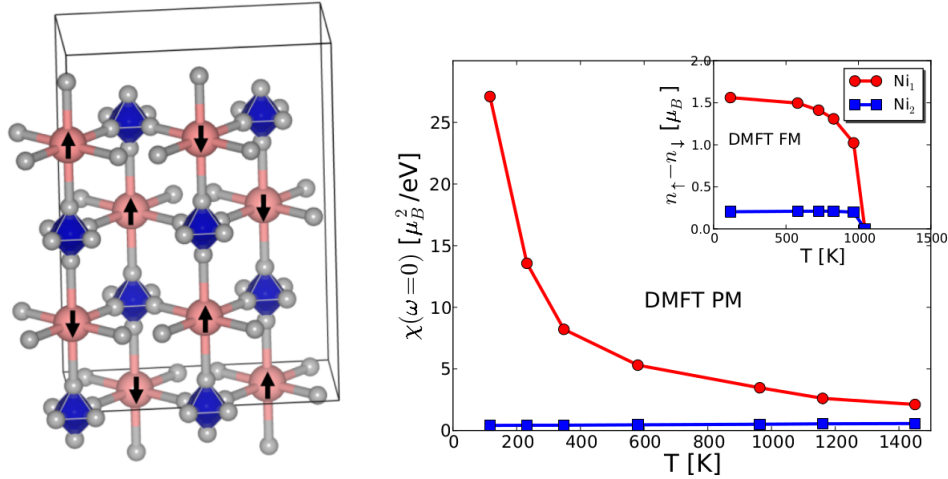**Figure 4.2:** Figure and caption from Park et al [40]. The local magnetic susceptibility $\chi(\omega=0)$ of LuNiO$_3$ calculated via DFT+DMFT as a function of temperature in the paramagnetic state using the low T P21/n structure with a mean bond length difference of 0.104 . Red circles, Ni1 (large Ni-O bond length). Blue square, Ni2 (small bond length). Inset: static magnetic moments from DFT+DMFT calculations.
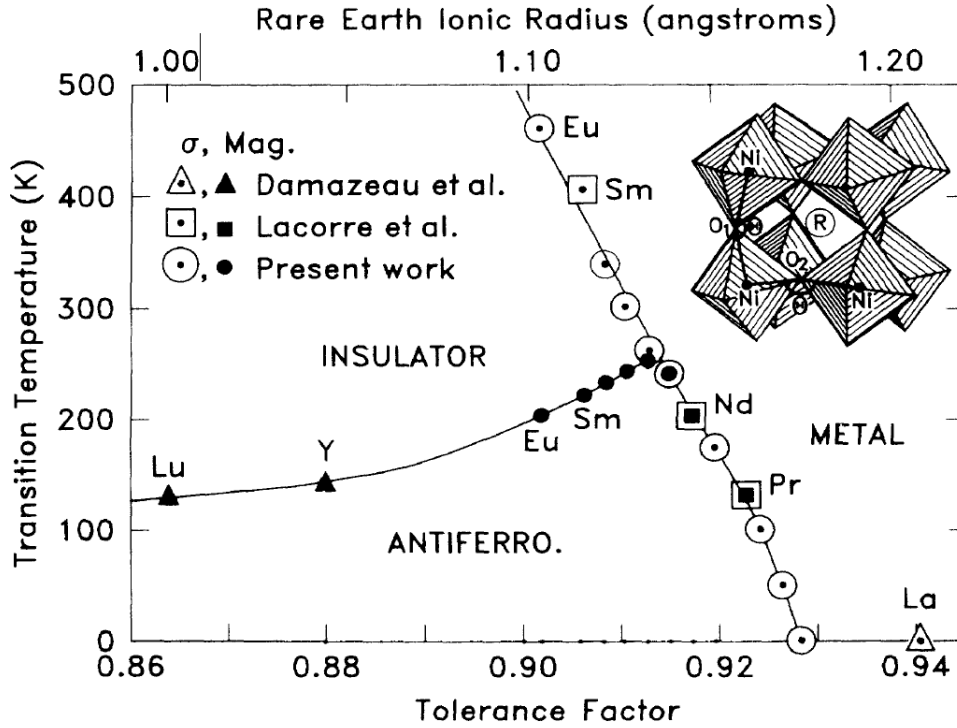
4.3   Phase Transitions

Figure 4.3:   Figure from J.B. Torrance [10]. Metal-Insulator and magnetic phase diagram for different RE Nickelates as a function of the tolerance factor or, equivalently the RE ionic radius.

Many substances have a complicated phase diagram with phase transition lines meeting a polycritical point. This cannot be explained in terms of a single order parameter theory [43]. It may be understood that the phase transition structure results from the interplay of more than one mode of ordering, that is, from the competition between two or more order parameters. Among systems exhibiting such behaviour are those showing competition between ferromagnetic and antiferromagnetic ordering [44] or between structural and magnetic orderings [45]. In the nickelate in particular we have a complex interplay between charge, spin and lattice degrees of freedom. The two electronic transitions characteristic of the insulating phase become stronger as we enter the magnetically ordered phase. This behavior is observed in all studied nickelates and is likely to be common to all nickelates. This change occurs at a temperature close to T_N. For this reason, we infer a tight relationship between electron spin and charge distribution in these materials. The following sections show how we tackle the problem of understanding such complex systems.

The presence of a soft-phonon mode associated with the NiO_6 octehedra which soften when temperature is lowered has been identified [46]. This softening is different for the $T_N = T_{AF}$ regime and the $T_N < T_{AF}$. Charge disproportionation alone is unlikely to induce a phonon mode

softening which support the idea of a intimate correlation charge spin and lattice degree of freedom

4.4   Landau Theory

The Landau theory (LT) of phase transition is a theoretical framework constituted by thermodynamics and symmetry considerations [47]. Based solely on symmetry considerations, the LT can provide a reliable description of the behavior of a system's equilibrium near a phase transition. Within the framework of the theory, the existence of a transition is an experimental fact considered as a starting point. LT is thus a phenomenological theory. It relates measurable quantities to one another using a minimum set of input parameters which can be determined either by comparison with experiment or from first-principle calculations. The explanatory power of this theory is to establish the overall consistency of the microscopic characteristics of the transition (space-symmetry and structural charges) and the results of the measurements of macroscopic quantities. Landau theory can therefor serve as a conceptual bridge between microscopic model and observed macroscopic phenomena [47]. Because it assumes spatial averaging of all local fluctuation, LT is particularly well suited to systems with long-range interactions such as superconductivity and ferroelectricity.

In his classic 1937 paper, Landau notes that a system cannot change smoothly between two phases of different symmetries [48] [49]. Furthermore, the thermodynamic states of two phases that are symmetrically distinct must be the same at their common transition line. For this reason, the symmetry of one phase must be higher than that of the other.

The Landau theory defines two basic concepts: the order parameter and the free energy F. The symmetry properties of these two quantities make it possible to infer on the one hand, symmetry characteristics of the system such as degeneracy of the "low-symmetry" phase. On the other hand, macroscopic quantities can be classified as a function of their relationship with the order parameter. The order parameter represents the degree of freedom which allows describing the symmetry and physical change accompanying the phase transition in a system. It is a physical entity that is zero in the high-symmetry (disordered) phase and changes continuously to a finite value once the symmetry is lowered. The key result of Landau theory is that the order parameter will take a non-zero value below the transition temperature T_c.

A central Ansatz of the Landau approach is that the free energy can be represented as a series expansion of the order parameter in the vicinity of the transition. If the order parameter is multicomponent, then the Landau free energy is constituted from all scalar terms consistent with the system's symmetries that are powers and scalar products of the order parameter components. In the next chapter, we will show how the free energy F, in the vicinity of the transition, is written as a Taylor expansion of the order parameter $F(p)$ with only the symmetry-compatible

terms. The function $F(p)$ is a variational free energy and not the equilibrium free energy of the system. The equilibrium value of the order parameter is defined as the one that minimizes the value of the variational free energy. Concerning the form of the variational free energy, one assumes that F is a continuous and derivable function of its variables (temperature, pressure and/or order parameters).

The central property of the variational free-energy is its symmetry: F is invariant by the symmetry transformation of the (high temperature) structure. The specific form of F thus determines the symmetries of the potentially stable phase below T_c. Is also determines the degeneracy of these phases as well as the temperature dependence of the relevant physical quantities.

With these tools in hand, we may ask ourself when does LT break down ? The power-law form of F is expected not to be valid very close to the transition [50] Furthermore LT is based on the premise that local fluctuations in the order parameter are small. This is expected that this will be the case far away from the transition. Levanyuk and Ginzburg have developed a criterion which uses Landau theory to estimate its own demise [51] [52]. Qualitatively their criterion suggests that LT works well when the dimentionality is large or the interaction are long-range.

4.4.1 Phenomenological Model for coupled magnetic and charge-order in the RE Nickelates

We write down the free energy F as a Taylor expansion of two order parameters: one for the charge-ordered phase (Φ) and another for the magnetic phase (m). This gives:

$$F = \sum_{n=0}^{\infty} A_n (B_n \Phi + C_n m)^n$$

Expanding the power series gives:

$$
\begin{aligned}
F = {} & A_0 \\
& + A_1 \left(B_1 \Phi + C_1 m \right) \\
& + A_2 \left(B_2 \Phi^2 + 2B_2 C_2 \Phi m + C_2 m^2 \right) \\
& + A_3 \left(B_3 \Phi^3 + 3B_3 C_3 \Phi^2 m + 3B_3 C_3 \Phi m^2 + m^3 \right) \\
& + \dots
\end{aligned}
$$

Concerning the symmetry of the order parameter, the magnetization vector field m represents the average of the elemental spin. Without a symmetry-breaking vector field such as a magnetic field, the Hamiltonian is symmetric against the inversion of the sign of m. For this reason, the Landau free energy is an even function of m. A similar argument holds for the charge-disproportionated order parameter Φ which represents the oxygen-breathing distortion of the NiO_6 octahedra as represented in Figure 4.4. When non-zero, the system is in the charge-disproportionated state with alternating long-bond (LB) and short-bond (SB) sites. The starting point of the alternance is set by the sign of Φ: We either have LB-SB-LB-SB or, for the opposite sign of Φ, SB-LB-SB-LB. As their relative position and their relative number remain identical, the Landau free energy remains the same. The free energy is then independent of the sign of Φ and is then an even function as well. For this reason, only the even terms of the expansion are considered here. Condensing the product of coefficient A_n, B_n and C_n into single parameters, we can write an already simplified version of the expansion:

$$
\begin{aligned}
F = F_0 \\
+ \alpha_\Phi \Phi^2 + \alpha_m m^2 \\
+ \beta_\Phi \Phi^4 + \beta_{Cpl} \Phi^2 m^2 + \beta_m m^4 \\
+ \gamma_\Phi \Phi^6 + \gamma_{Cpl1} \Phi^2 m^4 + \gamma_{Cpl2} \Phi^4 m^2 + \gamma_m m^6
\end{aligned}
$$

$$2\, BO_6 \qquad B\text{-site 1} \qquad B\text{-site 2}$$
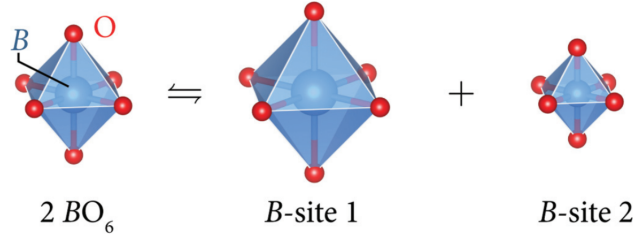
Figure 4.4: Figure from S. Ciuchi [21]. Illustration of the effect of charge disproportionation on the local BO_6 octahedral site. In the (paramagnetic) metallic state, all octahedra are equivalent. In the insulating state, the octahedra disproportionate into inequivalent sites. Charge-transfer between one nickel site to the other dilate one site while contract the other. Such configurations resemble a "breathing" mode

From this expression, we can proceed to some simplifications. On the one hand, as our data strongly suggest (Figure 5.1), we assume that the metal insulator transition is a first-order transition [9, 53]. Such transition involves the coexistence of two phases (discontinuous transition between charge-disproportionated states). For this reason, the free energy must present two minima. The sixth power is enough to produce this feature 4.6b). The power expansion of the Φ order parameter is then truncated at the sixth power. On the other hand,

the magnetic phase transition is assumed to be second order (continuous transition) meaning that only one minimum must be present in the free energy. The power expansion of the m order parameter is then truncated at the fourth term (4.6a).

If the coefficient of the highest order term of the expansion in m (or Φ) is negative, the most stable solution occurs for infinite m (or Φ). For this reason, the coefficient of the highest term of the expansion will always be positive. The stiffness of the "well" is controlled by the coefficient of the highest term. In order for the free energy to show a minimum away from 0, that is, in order for the system to reach an ordered phase, we must allow the coefficient of the lower terms to be negative. These two scenarios are represented in Figure 4.6

The coupling constants between the two order parameters β_{Cpl} and γ_{Cpl} quantify the dependence between the two different phases in our material. That is, how the charge-ordered phase influences the magnetic phase and reciprocally. For small values of the order parameters we can restrict the coupling terms to the lowest order one, i.e. we retain only the term proportional to $m^2\Phi^2$ and exclude those proportional to $m^2\Phi^4$ and to $m^4\Phi^2$. This biquadratic coupling has been used extensively already [54]. In order to terminate our simplification, we must consider the term in m^2 with care. If negative, this term signifies that the magnetic phase can occur without the charge-disproportionated phase. Our measurement however, shows that this is unlikely as the two peaks present in the optical conductivity spectrum in the magnetic phase are already present in the CD phase (Figure 5.1). They are the signature of the CD phase as shown by [42]. As these two peaks furthermore increase in the magnetic phase, we state that the CD phase is a condition sine-qua-non for the magnetic phase to appear and thus cannot occur alone. For this reason, we drop the term m^2 in our expression of the free energy.

We can thus write down the free energy expansion as:

$$F - F_0 = \alpha_\Phi \Phi^2 + \beta_\Phi \Phi^4 + \beta_C \Phi^2 m^2 + \beta_m m^4 + \gamma_\Phi \Phi^6$$

The occurrence of the magnetic phase is still possible in this expression via the mixed term $\beta_{Cpl}\Phi^2 m^2$ provided $\Phi \neq 0$. This term must furthermore be allowed to be negative, just like the lower term of the expansion in Φ. For this reason, we chose α_Φ and β_{Cpl} to be temperature dependent with the form:

$$\alpha_\Phi = \alpha_0 \left(\frac{T}{T_{MIT}} - 1 \right)$$
$$\beta_{Cpl} = \beta_0 \left(\frac{T}{T_N} - 1 \right)$$

Figure 4.5 a) shows the simulated behavior of the two coupled order parameters. As we cool down, the CD phase appears first and then the magnetic phase. As we continue to cool down

we observe a change in behavior of Φ. Its curvature, shown in Figure 4.5 b), becomes positive at about 100 K. This behavior is associated with the coupling constant β_{Cpl}. This mimics the behavior of $\sigma_1(T)$ that shows a kink around T_N in the two samples where the two transitions occur at different temperature. This is an indication that the two phases in our sample are indeed entangled.
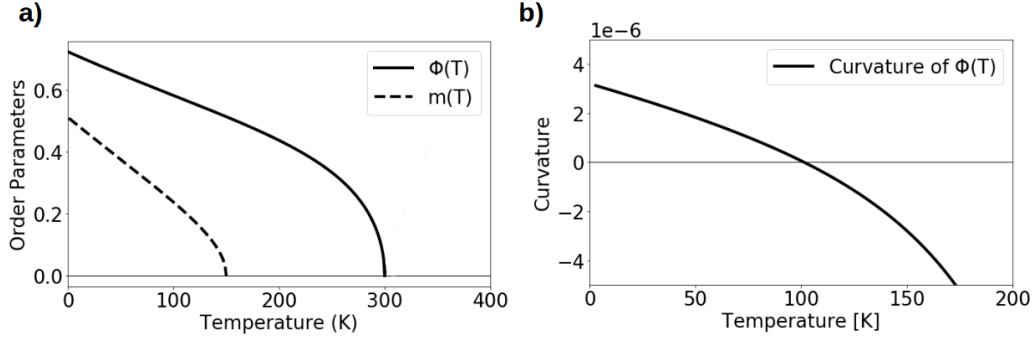

Figure 4.5: a) Temperature dependence of the two coupled order parameters. In this example, we wrote the free energy expansion using the following parameters: $\alpha_0 = 20$, $\beta_0 = 15$, $\beta_m = 5$, $\beta_\Phi = 5$ and $\gamma_\Phi = 2$. The two critical temperatures T_N and T_{MIT} can be read on the graph and are 150 and 300 respectively. b) Curvature of the order parameter associated with the charge-disproportionation as a function of the temperature.

To further investigate the behavior of our model, the evolution of the free energy calculated using the chosen parameter is shown in Figure 4.7. At low temperature, we have a steep energy well located at about $(m, \phi) \sim (1,1)$. The minimum is well below zero with already a tendency toward the non-magnetic phase (toward $m = 0$). This tendency is indeed confirmed in the free energy surface at T_N where the minimum is now more flat. We now see a tendency toward the metallic phase (toward $\Phi = 0$). Finally, at T = 350 K well above the two critical temperatures, the system is driven toward $(m, \phi) \sim (0,0)$. At this high temperature, we can see that the energy-well is now quit flat compared to the one at low temperature. The evolution of the free energy with the temperature reproduces the behavior expected from the phase diagram [55]. We are thus confident that this model can be used to shine some light on the entanglement between the charge disproportionated and the magnetic phase. In the section on the data analysis, I will thus go into more detail about this model and how to use it to interpret our measurements.
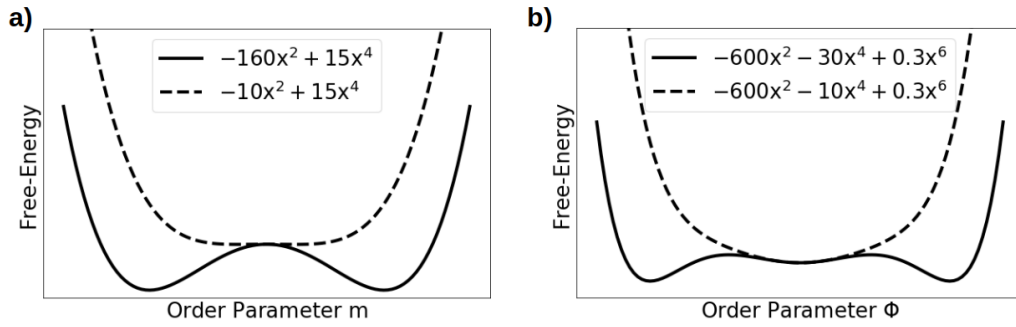
Figure 4.6: Representation of the free energy as a Taylor expansion of the order parameter. a) Second-order (continuous) phase transition. As the coefficient of the x^2 term is varied, the system goes smoothly from a non-zero order parameter to zero. b) First-order (discontinuous) phase transition. The presence of two minima is possible due to the negative coefficient of x^2 and x^4.
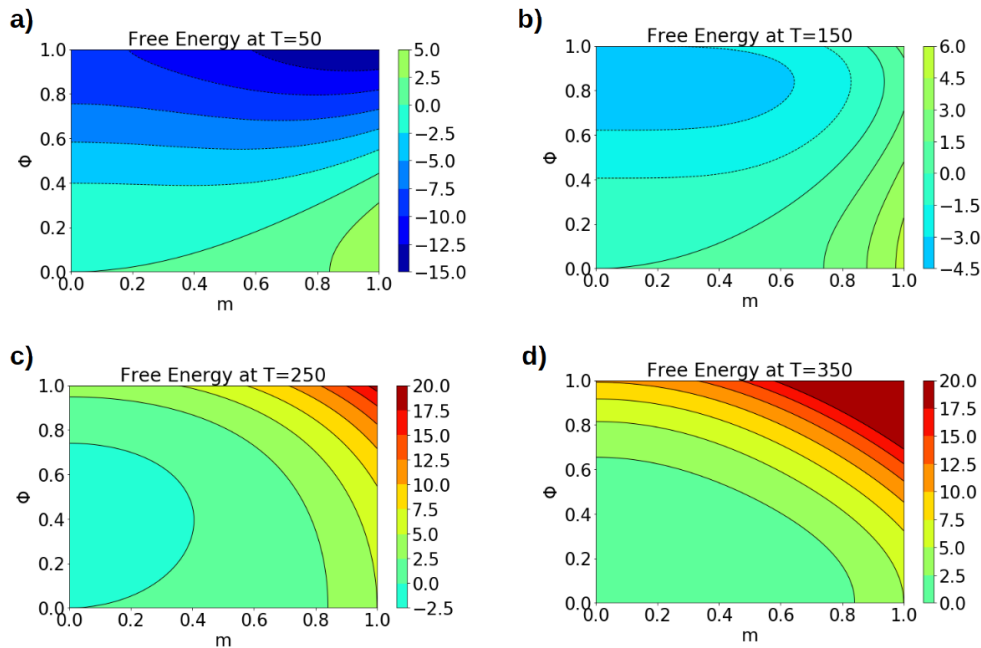
Figure 4.7: Contour plots of the Landau free energy as a function of the two order parameters at four different temperatures. a) Insulating, antiferromagnetic phase b) insulating phase at T_N c) insulating paramagnetic phase and d) metallic paramagnetic phase

5

Optical spectroscopy and the nature of the insulating state of rare-earth nickelates

In this chapter I present optical data of RENiO$_3$ for different compositions, show the detailed temperature dependence of the spectra, and demonstrate how these optical spectra are related to the electronic structure of the paramagnetic metal state and the bond disproportionated insulator state. I also show that the peak intensity is a measure of the charge disproportionated phase. The presence of a double peak is characteristic of the insulating phase [41, 56]. Second we show how this phase is coupled with the magnetic phase: As the intensity of the two peaks in the optical conductivity spectrum scales with the degree of charge disproportionation, we stated that the optical conductivity is an indicator of the order-parameter associated with bond-disproportionation [57]. Furthermore, as it couples with the magnetisation order parameter, we see a change in the behaviour of σ_1 at the Néel temperature. For this reason, we were able to probe the magnetic order using optics. In this section, we provide experimental evidence of the coupling between magnetic order and charge-disproportionated state. We explain this coupling within the framework of Landau theory of phase transition.

This chapter has been adopted with small modifications from Physical Review B 92, 155145 (2015), J. Ruppen, J. Teyssier, O.E. Peil, S. Catalano, M. Gibert, J. Mravlje, J.-M. Triscone, A. Georges & D. van der Marel.

5.1 Introduction

The rare earth nickelates RNiO$_3$ form a remarkable group of materials [?, 10, 33, 55]. While LaNiO$_3$ remains metallic down to very low temperatures, all other nickelates undergo a metal-insulator phase transition (MIT) and antiferromagnetic (AF) ordering as the temperature is lowered. The two transitions coincide for Pr and Nd but they are distinct, with $T_{\mathrm{AF}} < T_{\mathrm{MIT}}$, for all rare-earth cations smaller than Nd (Sm, Gd, and so on down to Lu) [33]. The mechanism

of this MIT, which differs from that of a homogeneous Mott transition, raises questions of fundamental importance. Furthermore, the possibility of controlling the MIT by chemical substitutions, strain, heterostructures, gating or light pulses [**?**, 33, 55, 58–60] makes these materials particularly interesting for potential applications. For those reasons, nickelates have recently been the subject of intensive research and attention.

The insulating phase is characterized by a lowering of the crystal symmetry from orthorombic to monoclinic and by a disproportionation of Ni-O bond lengths: the NiO_6 octahedra undergo a breathing distortion, with alternating long-bond (LB) and short-bond (SB) octahedra on each sublattice. This lattice modulation is accompanied by some form of charge-ordering, the precise nature of which has been the subject of debate. Early work [39, 61] emphasized the formation of ligand-holes, and the importance of the $d^8 \underline{L}$ local configuration, in contrast to the d^7 configuration corresponding to the nominal Ni^{3+} valence. This leads to a physical picture for the charge-ordering in which Ni-O bonds are involved (rather than Ni atomic sites). In an extreme limit of this picture, LB octahedra are associated with the d^8 configuration (with a large local moment) and SB ones with $d^8 \underline{L}^2$ (with the Ni local moment screened by the two ligand holes) [25, 40]. Recently, theoretical work has provided support to this physical picture: in Ref. [40] the MIT was explained as a 'site-selective' Mott transition associated with the d^8 LB sites, and in Ref. [42] a corresponding low-energy description was proposed, focusing on the strongly hybridized Ni-O states with e_g symmetry.

In this description, consistently with the proposal of Ref. [62], an effectively attractive interaction between electrons with parallel spins in different orbitals naturally leads to the formation of a bond density-wave. Since the bands are quarter filled, the corresponding doubling of the unit cell opens a gap *above* the Fermi level, leaving the material metallic at the band-structure level. The observed insulating state results in fact from the *combination* of unit cell doubling and Mott physics (local moments) at the LB sites. Although a consistent picture of the MIT appears to be emerging, a direct comparison to experiments is still lacking.

In this paper, we report experimental optical spectra on three different nickelate systems. These spectra show a common feature: the appearance of two peaks as the MIT is crossed - hence a 'universal' feature of the MIT. We show that this provides direct insight into the structure of the insulating phase, and that the 2-peak structure results from the bond-disproportionated nature of the low-T phase, with two kinds of nickel sites. We perform dynamical mean-field theory (DMFT) calculations within the theoretical framework introduced in Ref. [42], which are found to reproduce quite well the main features of the optical spectra. Based on these calculations, we provide a simple analytical understanding of these main features, and of the relative roles of the Peierls and Mott mechanisms in the MIT of nickelates.
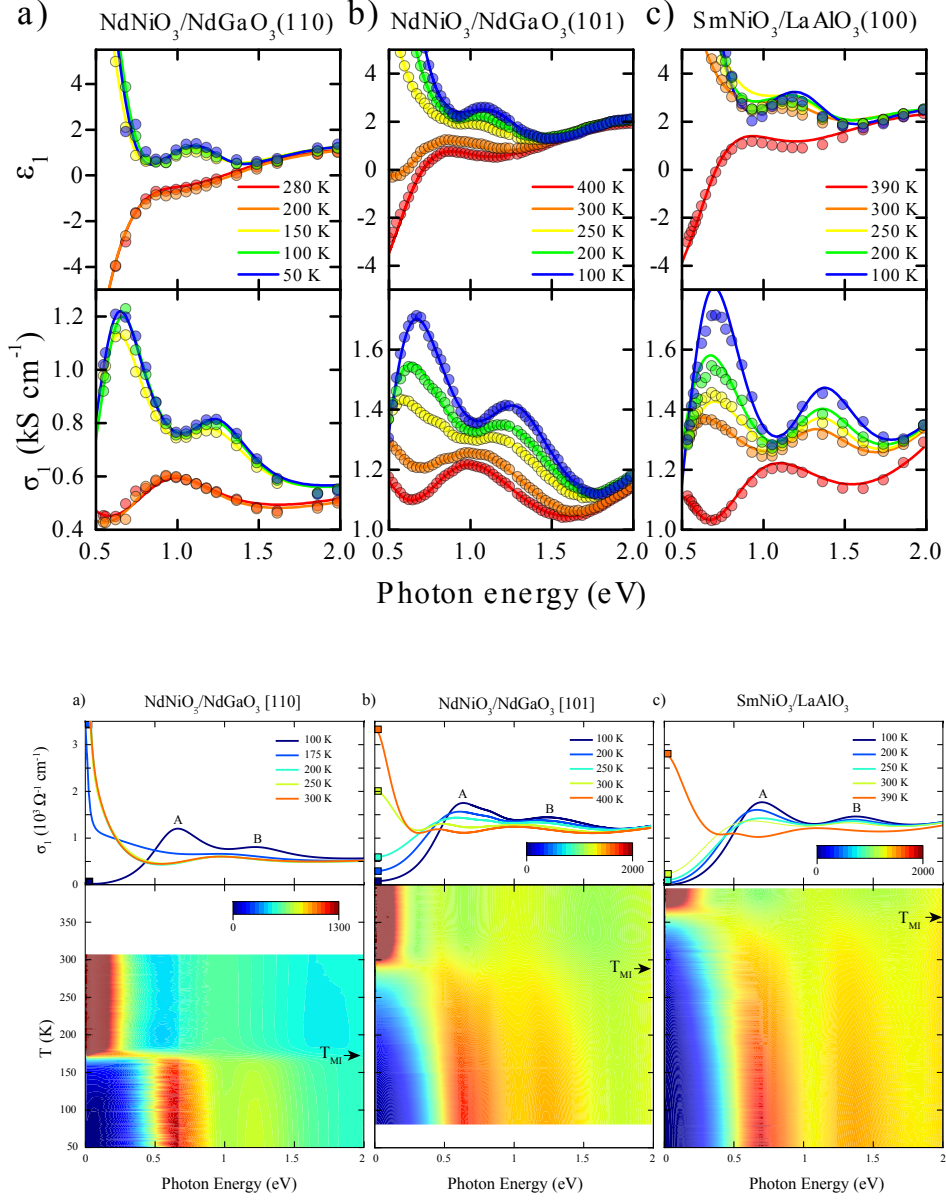
Figure 5.1: Top) Real part of the dielectric function (first row) and optical conductivity (second row) of NdNiO$_3$ on a NdGaO$_3$ (110) substrate (left), NdNiO$_3$ on a NdGaO$_3$ (101) substrate (middle) and for SmNiO$_3$ on a LaAlO$_3$ (100) substrate (right). Bottom) Real part of the optical conductivity for selected temperatures and energy/temperature color maps of samples a) NNO/NGO-110, b) NNO/NGO-101 and c) SNO/LAO-001. Metal-insulator phase transitions are indicated by arrows on the colormaps. *A* and *B* designate two peaks in the insulating phase. Data at 0 eV come from DC measurements.

5.2 Experiment

Scanning tunneling microscopy [63] and Terahertz time-domain [64] spectroscopy experiments have been interpreted as evidence of a charge-density wave formation. Previous optical studies of $NdNiO_3$ films have already shown that in crossing from the correlated metalllic (mass enhancement of order 4 [65, 66]) to the insulating phase strong peaks appear at approximately 0.5 eV and 1.0 eV [41, 67]. The Drude spectral weight is redistributed up to at least 5 eV when the system becomes insulating [41, 67, 68], which was interpeted as an indication of Mott physics [41] or effects of electron-phonon interaction [68]. However, a clear mechanism of the optical response of the insulating phase has thus far been lacking.

The following thin film/substrate combinations were used in the present study: $NdNiO_3$ on an (110) oriented $NdGaO_3$ substrate (NNO/NGO-110)[1], $NdNiO_3$ on $NdGaO_3$ (101) (NNO/NGO-101) and $SmNiO_3$ on $LaAlO_3$ (001) (SNO/LAO-001). These high quality epitaxial films were prepared as described in Refs. [69, 70]. The dielectric function was determined in the range from 0.5 and 2 eV using ellipsometry at a reflection angle between 65 and 72 degrees with the surface normal.

Measurements were performed in steps of 1 K using a special UHV cryostat with a vacuum better than 10^{-9} mbar. Data of substrate films and substrates were combined to calculate the complex dielectric function, $\epsilon(\omega) = \epsilon_1(\omega) + i4\pi\sigma_1(\omega)/\omega$, using the Fresnel relations. The resulting thin film dielectric functions for all three samples are presented in Fig. 5.1 for a limited set of temperatures.

DC resistivities of the films were measured as a function of temperature using the four terminal method. Drude Lorentz-fitting to the DC resistivity (symbols at zero energy in Fig. 5.1) and the complex dielectric function from 0.5 to 2 eV was used to interpolate the optical data below 0.5 eV. While the spectral weight of $\sigma_1(\omega)$ integrated from 0 to 0.5 eV is accurately represented by this procedure due to the constraints imposed by simultaneously fitting $\sigma_1(\omega)$ *and* $\epsilon_1(\omega)$ [71], fine details such as phonons are not captured in this representation. Figure 5.1 shows the energy dependence (upper panels) and energy/temperature color maps (lower panels) of the real part of the optical conductivity for samples NNO/NGO-110 (a), NNO/NGO-101 (b) and SNO/LAO-001 (c). In the insulating state, at low temperatures, the dominant features of the optical conductivity are two peaks at 0.6 (*A*) and 1.4 eV (*B*) for all three samples (Fig. 5.1 a-c). Upon increasing the temperature and passing through the insulator-metal transition, the peaks vanish and a broad 1 eV peak along with a weak feature at 0.5 eV for samples (b) and (c) appear instead. Formation of free carriers is clearly visible with the growth of a zero energy mode in the optical conductivity for $\hbar\omega \lesssim 1$ eV (Fig. 5.1) and a sign change in the real part of the dielectric function (Fig. 5.1).

---

[1]Note that $NdGaO_3$ is orthorhombic, and that we employ the corresponding notation for the crystal planes.The (110) and (101) planes of $NdGaO_3$ correspond to $(001)_{pc}$ and $(111)_{pc}$ in pseudo-cubic notation.
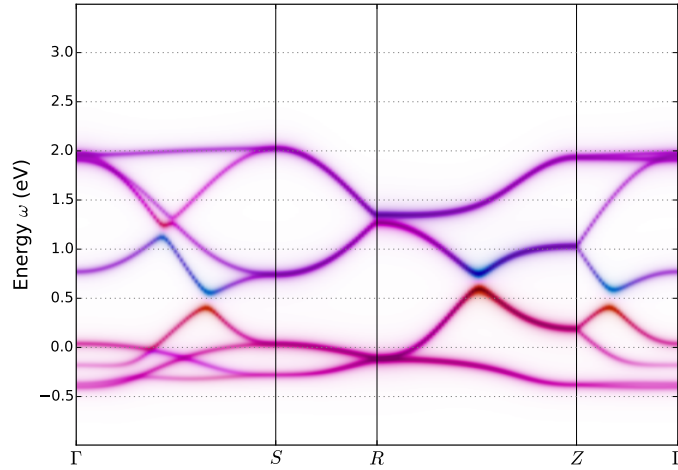
Figure 5.2: The bare (GGA) band structure of the monoclinic phase of SmNiO$_3$. The color represents the site character of the states: LB (red) and SB (blue). Note the Peierls splitting at an energy +0.5–0.7 eV. The position of the Fermi level is $\varepsilon = 0$.

From the metallic to the insulating state, all three samples present a comparable amount of spectral weight, of approximately 3 eV^2, which is transferred from the region below 0.5 eV (representative of the free carriers in the system) to higher energy range which extends to at least 5 eV pointing to strong correations in the insulating state [41].

5.3 Theoretical calculations

To understand the nature of the optical excitations observed experimentally, we have performed DMFT calculations for the bulk low-T phase of SmNiO$_3$ (space group $P2_1/n$), within the low-energy framework introduced in Ref. [42]. This approach involves only the states with e_g symmetry resulting from the anti-bonding combinations of Ni-3d and O-2p states. At the band-structure level, this corresponds to eight bands, reflecting the four Ni-sites per unit cell with two e_g states per site, and a total occupancy of 4 electrons per unit cell (one per site on average). The bare (GGA) band structure of monoclinic SmNiO$_3$ is displayed in Fig. 5.2. The bands with e_g character form a well-isolated set of bands of total bandwidth $\simeq$ 2.3 eV, separated by a gap of $\sim 0.5 eV$ from the low-lying t_{2g} and oxygen states (not shown on Fig. 5.2). At the LDA/GGA level, these materials are metallic in both the orthorhombic and monoclinic structure, with the Fermi level crossing the e_g manifold. As clearly seen on Fig. 5.2, the breathing distortion (bond disproportionation) in the monoclinic structure leads to the opening of a Peierls-like gap in the energy-range $0.5 - 0.7$ eV. This gap separates 4 lower-lying bands with dominantly LB character and four higher-lying bands with dominantly SB character. Due do the breathing distortion of the low-T phase the local on-site energies of LB and SB sites are split by $\Delta_s \simeq 0.25$ eV. This in

43

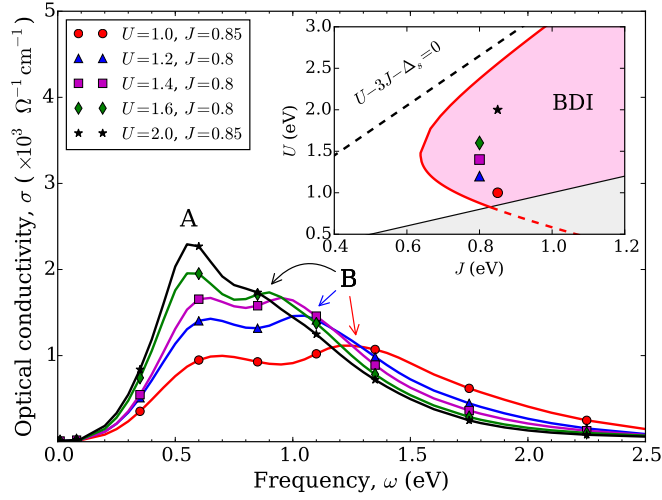## 5. OPTICAL SPECTROSCOPY AND THE NATURE OF THE INSULATING STATE OF RARE-EARTH NICKELATES

Figure 5.3: Calculated optical spectra for several values of U and J. The two peaks are denoted by A (constant position) and B (varying position). Inset: Phase boundary of the bond-disproportionated insulating state. The symbols indicate the values of U, J, chosen such that the leading edge is kept approximately constant of order 0.5 eV.

turn results in the opening of a Peierls-like gap in the band-structure (of magnitude $\sim \Delta_s$) at an energy of order $+0.5$ eV above Fermi level corresponding to half-filling (two electrons per site). This Peierls mechanism alone is therefore insufficient to account for the insulating nature of this phase, and correlations play an essential role.

As was demonstrated in Ref. [42], considering the Coulomb repulsion U and Hund's coupling J acting within the set of e_g states allows one to describe the MIT provided that $U - 3J \lesssim \Delta_s$. As illustrated on the partial phase diagram in the inset of Fig. 5.3, a 'bond-disproportionated insulator' (BDI) phase is found in this regime, in which the e_g occupancy is modulated, with a smaller value on the SB sites and a larger one on the LB sites. Orbital polarization is weak in this BDI state, with both e_g orbitals approximately equally occupied on each site.

We applied an *ab initio* LDA+DMFT approach to the low-T phase of $SmNiO_3$ and calculated the electronic spectral functions and the optical conductivity using the Kubo formalism. We display in Fig. 5.3 the calculated optical spectra, for a set of values of U and J within the BDI phase. The values, indicated in the inset of Fig. 5.3, are chosen in such a way that the leading edge is roughly constant and close to the observed experimental value (~ 0.5 eV). In agreement with experimental data, all the theoretical spectra demonstrate the presence of two peaks (denoted by A and B in the figure). While the position of peak A is fixed by the choice of parameters, both the position of peak B and its relative intensity increase as one moves from the upper to the lower boundary of the phase diagram, *i.e.* as $U - 3J$ becomes more negative and the disproportionation increases.

To identify the optical transitions associated with these two peaks, we display in Fig. 5.4 the

momentum-resolved spectral functions plotted for the two extreme points (both at $J = 0.85$ eV): $U = 2.0$ eV (smaller disproportionation) and $U = 1.0$ eV (larger disproportionation). Three sets of states can be identified, split by a correlation-induced indirect gap at the Fermi level and by a pseudo-gap (originating from the Peierls LB/SB site modulation) at around +0.5 eV. The Peierls pseudo-gap is clearly seen in the density of states (side panels of Fig. 5.4) and the momentum locations at which it opens are indicated by circles in the main panel. The states below Fermi level always have dominant LB character, in accordance with the largest occupancy of LB states. In contrast, the nature of the lowest unoccupied band immediately above the gap changes from dominantly LB at $U = 1$ eV to dominantly SB at $U = 2$ eV.

The optical transitions responsible for the lower-energy peak *A* are the ones across the insulating gap, while the second peak is due to optical transitions across the Peierls pseudo-gap, as indicated by arrows on Fig. 5.4. The current operator has only inter-site matrix elements, with largest nearest-neighbor components coupling sites with different characters. This explains why the first peak has higher relative intensity when the states on either side of the gap have different characters, *i.e.* on the upper side of the BDI phase boundary (smaller disproportionation).

5.4 Analysis and discussion

Fig. 5.4 reveals that the dominant site character of the lowest unoccupied states above the gap is different for the two values of U. Specifically, it is LB-like for $U = 1.0$ (corresponding to the lower part of the BDI region in the phase diagram) and SB-like for $U = 2.0$ (upper part). To understand better the electronic structure and, in particular, the structure of unoccupied states we first note that the self-energies in the BDI phase can be well described at low energy by

$$\Sigma'_{\text{SB}}(\omega) - \mu = \varepsilon_{\text{SB}} \qquad\qquad \Sigma'_{\text{LB}}(\omega) - \mu = \frac{\delta^2}{\omega - \varepsilon_p} + \varepsilon_{\text{LB}} \qquad (5.1)$$

These expressions have a simple physical meaning. The lower occupancy SB sites are weakly correlated and hence have an approximately constant self-energy. The LB sites, in contrast, have a self-energy typical of a Mott insulator, with a pole-like divergence at $\omega = \varepsilon_p \simeq 0$ which is responsible for the opening of the insulating gap (with a magnitude controlled by the energy scale δ). This is consistent with the 'site-selective Mott' picture of Ref. [40].

Simplifying further, let us consider a model with only two sites (LB and SB) per unit cell and nearest-neighbor hopping $t_{\mathbf{k}}$, so that the non-interacting Hamiltonian reads:

$$H^0_{\mathbf{k}} = \begin{bmatrix} \varepsilon^{(0)}_{\text{LB}} & t_{\mathbf{k}} \\ t^*_{\mathbf{k}} & \varepsilon^{(0)}_{\text{SB}} \end{bmatrix}, \qquad (5.2)$$
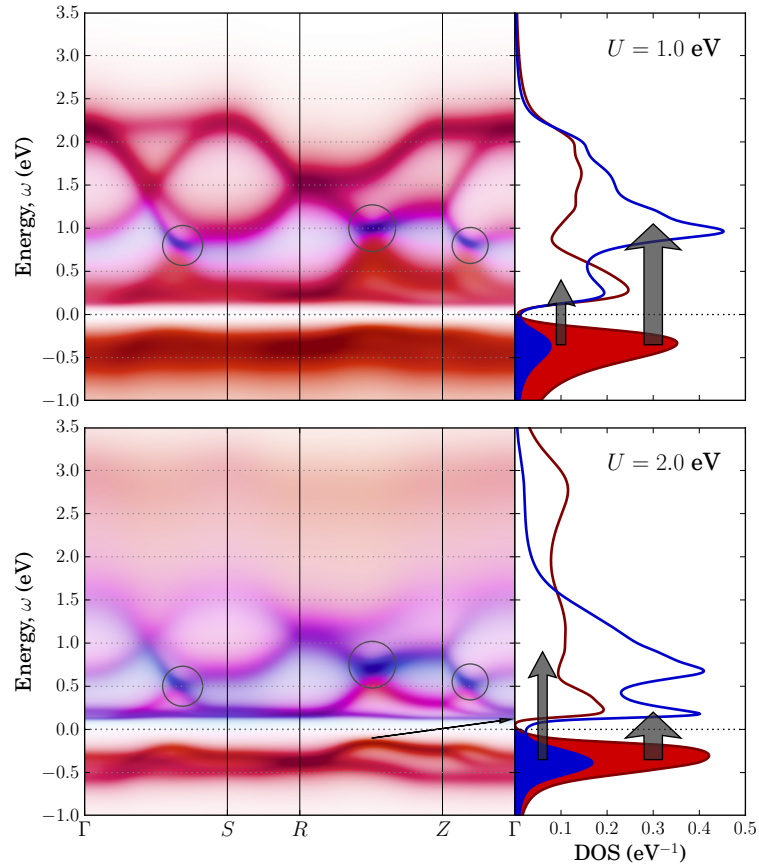
Figure 5.4: Momentum-resolved spectral function (color intensity map) for two selected parameter sets: $U = 1.0$ eV, $J = 0.85$ eV (top) and $U = 2.0$ eV, $J = 0.85$ eV (bottom). The colors represent the site character of a state: red for LB, blue for SB (violet for a mixed LB/SB character). A darker (lighter) tone corresponds to higher (lower) spectral intensity. The circles indicate the energy-momentum locations where the Peierls pseudo-gap opens. The indirect Mott-like gap is indicated by the black arrow connecting the highest occupied states between R and Z and the lowest unoccupied states at Γ-point. Side-panel: momentum-integrated spectral functions (density of states) for LB (red) and SB (blue) sites, with arrows indicating the optical transitions corresponding to the two peaks (see text).

Figure 5.5: Left-hand side of the quasi-particle equation Eq. (5.3) and graphical construction of the three QP branches. The green (shaded) area shows the region of allowed values of the RHS: $0 \leq |t_k|^2 \leq W^2/4$, where W is the bandwidth. ω_i, $i = +, -$, and $\omega = \varepsilon_{SB}$ are the root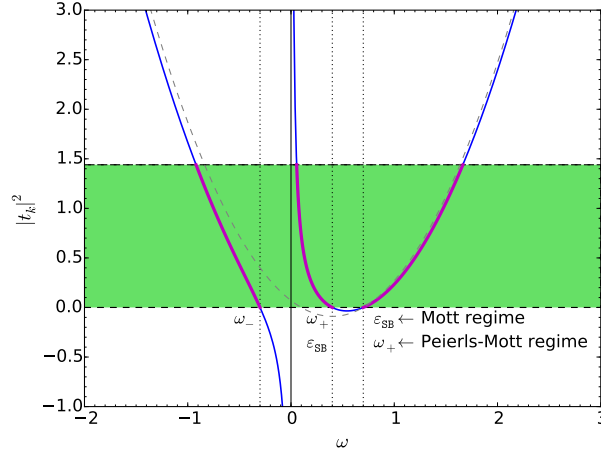s of the equation for $t_k = 0$. The order of the roots ω_+ and ε_{SB} depends on the regime (Mott or Mott-Peierls, see text).

The dispersion, $\omega = \omega_{\mathbf{k}}$ of quasiparticles (QP) is then determined from the zeros of the determinant of $\omega + \mu - H_{\mathbf{k}}^0 - \hat{\Sigma}(\omega)$, leading to ($\varepsilon_p$ is neglected below):

$$\left(\omega - \varepsilon_{LB} - \delta^2/\omega\right)\left(\omega - \varepsilon_{SB}\right) = |t_{\mathbf{k}}|^2, \tag{5.3}$$

where $\varepsilon_{LB,SB} = \varepsilon_{LB,SB}^{(0)} - \mu + \Sigma_{LB,SB}^\infty$. This cubic equation has three QP branches, which are displayed on Fig. 5.6 for a simple one-dimensional tight-binding band $t_{\mathbf{k}} = W(1 + e^{i2ka})/4$ (with W the bandwidth).

To analyze this equation we plot the LHS as a function of ω, as depicted in Fig. 5.5, bearing in mind that the allowed states are limited by the range of values of the RHS, $0 \leq |t_k|^2 \leq W^2/4$. (The plot is done for $\varepsilon_{SB} > 0$, since the BDI state has site occupancies $n_{LB} > n_{SB}$.) From the figure we immediately see that the Mott gap at around zero frequency is an indirect one, as expected, and the Peierls gap is direct. For $k = \pm\pi/2a \equiv k_P$, which is the Fermi momentum of the half-filled system at which the Peierls gap opens, one has $t_{\mathbf{k}} = 0$ and the three roots read:

$$\omega_- = \frac{1}{2}\left(\varepsilon_{LB} - \sqrt{\varepsilon_{LB}^2 + 4\delta^2}\right), \tag{5.4}$$

$$\omega_+ = \frac{1}{2}\left(\varepsilon_{LB} + \sqrt{\varepsilon_{LB}^2 + 4\delta^2}\right), \tag{5.5}$$

$$\omega = \varepsilon_{SB}. \tag{5.6}$$

The occupied QP states correspond to $\omega_- < 0$ and have predominantly LB character. The insulating gap is always indirect, corresponding to transitions between the top of the occupied
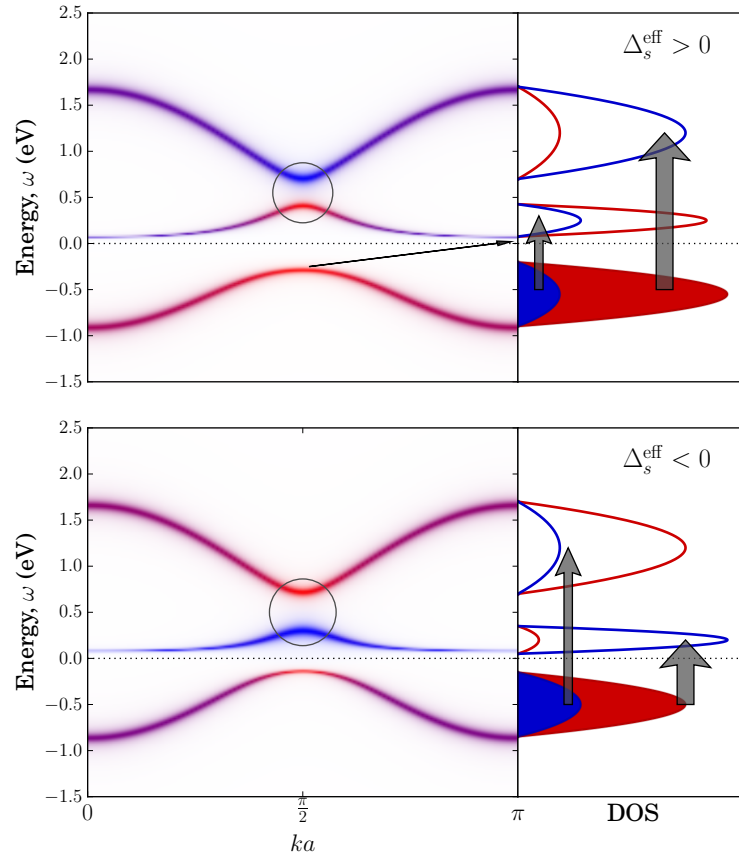
Figure 5.6: Quasiparticle band structure, density of states and main optical transitions of the simple model discussed in the text. Top: Mott regime, bottom: Mott-Peierls regime. Colors indicate the LB/SB character, as above. The indirect Mott-like gap is indicated with the thin arrow in the main panel.

band at $k = k_P$ and the bottom of the lowest unoccupied band at $k = 0$ (Γ-point). It can be estimated as:

$$\Delta_g \simeq \frac{4\delta^2 \varepsilon_{SB}}{W^2} + \frac{1}{2}\left(\sqrt{\varepsilon_{LB}^2 + 4\delta^2} - \varepsilon_{LB}\right) \tag{5.7}$$

Note that it vanishes for $\delta = 0$ as expected.

The nature of the lowest unoccupied branch above the insulating gap depends on the sign of:

$$\Delta_s^{\text{eff}} = \varepsilon_{SB} - \omega_+ = \varepsilon_{SB} - \frac{1}{2}\left(\varepsilon_{LB} + \sqrt{\varepsilon_{LB}^2 + 4\delta^2}\right) \tag{5.8}$$

whose magnitude $|\Delta_s^{\text{eff}}|$ is the Peierls direct gap renormalized by correlations, which separates the two unoccupied branches and opens at $k = k_P$ (as indicated by circles in Fig. 5.6). For $\Delta_s^{\text{eff}} > 0$ the lowest branch of unoccupied states has dominantly LB character: this corresponds to the regime of large disproportionation in which the almost half-filled LB band undergoes a Mott transition (top panels of Fig. 5.4 and Fig. 5.6, corresponding to the lower boundary of the BDI phase). For $\Delta_s^{\text{eff}} < 0$ the situation is reversed, and the states above the insulating gap are dominantly SB (bottom panels in Figs. 5.4, 5.6; corresponding to the upper boundary of the BDI phase with smaller disproportionation). In this 'Mott-Peierls' regime, the Mott mechanism has pushed the upper Hubbard band above the unoccupied band of SB states, and the states on either sides of the insulating gap have different characters (analogously to what happens in a charge-transfer insulator). Relative intensity and separation of the two peaks in the experimental data, suggest that the nickelates studied here may be more in the Mott-Peierls regime or in the crossover between the two regimes.

5.5 Conclusions

In summary, using ellipsometry we have measured the detailed temperature dependence of the optical conductivity spectra of strained $RNiO_3$ epitaxial thin films. The insulator is characterized by the occurrence of a conspicuous double-peak structure. *Ab initio* calculations and model considerations indicate that this optical signature reveals the peculiar structure of the insulating state suggested earlier [25, 40, 42]. Specifically, the two peaks in the optical conductivity of the insulating phase can be assigned to transitions from the lower Hubbard band to unoccupied bands split by a renormalized Peierls gap. Moreover, the model reveals two possible regimes with the lowest unoccupied states being of either LB or SB character, with the considered nickelate systems being close to the crossover between the two regimes. This provides another possibility of tailoring the properties of these materials by controlling the charge carrier density via stoichiometry or heterostructure engineering.

5. OPTICAL SPECTROSCOPY AND THE NATURE OF THE INSULATING STATE OF RARE-EARTH NICKELATES

Chapter 6

Impact of antiferromagnetism on the optical properties of rare-earth nickelates

In this chapter I demonstrate the connection between the optical spectra and the magnetic state of the RE nickelate. This chapter has been adopted with small modifications from Physical Review B 96, 045120 (2017), J. Ruppen, J. Teyssier, I. Ardizzone. O. E. Peil, S. Catalano, M. Gibert, J. M. Triscone, A. Georges & D. van der Marel.

6.1 Introduction

Rare earth nickelates form a class of transition metal oxides that undergo a metal-insulator transition as a function of the temperature T, and the so-called tolerance factor, t, which describes the distortion of the crystal structure associated to tilting and rotations of the oxygen octahedra surrounding the Ni-atoms. Depending on t that can be tuned by rare earth radius or strain, the material (i) remains metallic for all temperatures, (ii) switches in a first order phase transition to an antiferromagnetic insulator at T_{MI}, or (iii) traverses two phase transitions, the highest one at T_{MI} being from metal to paramagnetic (PM) insulator, and the lowest one being the Néel temperature T_N where the material becomes antiferromagnetic (AF). The insulating phase of rare-earth nickelates is understood in terms of inequivalent nickel sites. In an extreme picture, every second nickel site is in a d^8 configuration and carries a magnetic moment while the other ones are in a non-magnetic $d^8\underline{L}^2$ configuration [25, 26, 39, 40, 42, 72]. Due to electron-lattice coupling the long-range charge order (CO) is accompanied by a breathing lattice distortion [62, 73] opening a Peierls gap in the energy range 0.5-0.7 eV above the Fermi energy [42, 57]. The magnetically ordered phase is characterized by a wave-vector $\mathbf{k} = (1/4,1/4,1/4)$ [74] in pseudocubic notation. Two magnetic structures were proposed to explain the magnetic origin of this diffracted intensity: up-up-down-down [74] and non collinear ordering [75]. More recent measurements confirm the non-collinear structure [76].
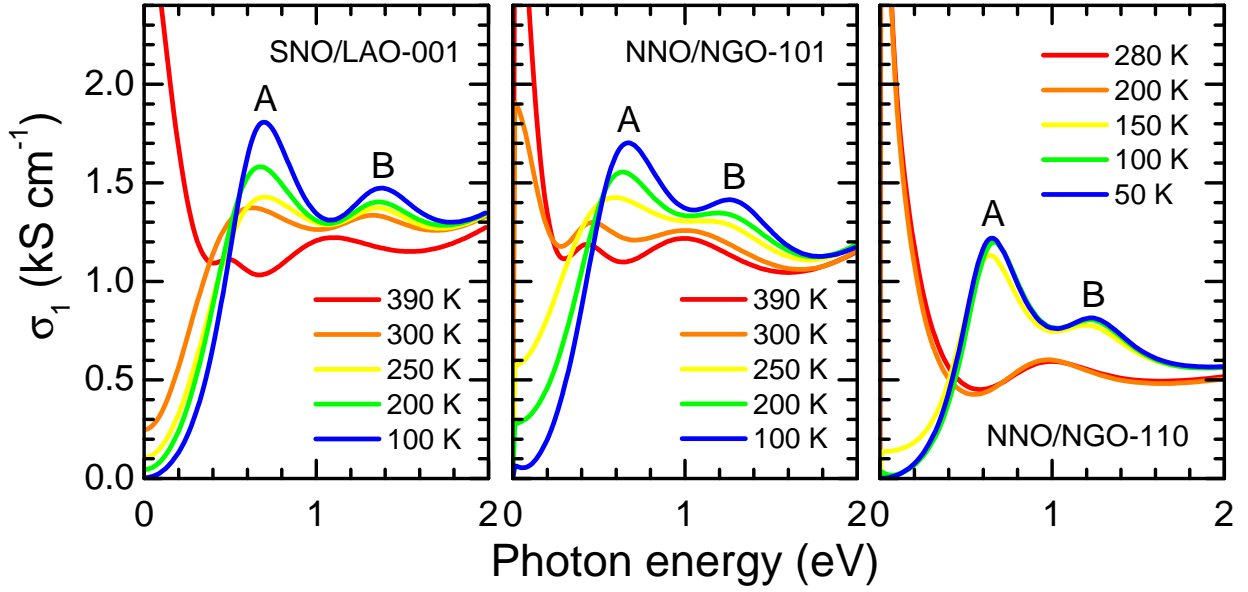
Figure 6.1: Optical conductivity spectra for selected temperatures of $SmNiO_3$ on a $LaAlO_3$ (001) substrate, $NdNiO_3$ on $NdGaO_3$(101), and $NdNiO_3$ on $NdGaO_3$(110) [57].

The relationship between the charge- and the magnetic order is still under debate. The optical conductivity in the insulating phase of $RNiO_3$ is characterized by two strong peaks at 0.6 eV and 1.3 eV (peaks A and B respectively) [57, 66, 77] (Fig. 6.1). In a recent paper we have reported the changes of the optical conductivity spectrum of $SmNiO_3$ and $NdNiO_3$ films [57], and compared the spectra in the metallic and insulating states. The aforementioned features of the optical spectra were found to be well reproduced by Dynamical Mean Field Theory (DMFT) calculations, allowing the identification of two peaks at 0.6 and 1.3 eV as the transitions across the Mott-insulating gap and the Peierls pseudogap respectively. The optical conductivity in the metallic phase is characterized by a zero-energy mode and a peak at 1 eV.

Here we report on the impact of AF order on the optical conductivity spectrum. We observe that antiferromagnetism in $SmNiO_3$ and $NdNiO_3$ thin films strongly influences peaks A and B, and causes an enhancement of the oscillator strength of these two peaks. The observed temperature dependence corresponds to a soft onset at the Néel temperature, signaling a positive reciprocal feedback between AF and charge order. Hysteresis of the optical spectra is strong when AF and charge order occur simultaneously, and negligible when these occur at separate temperatures, consistent with Refs. [33, 55, 59, 60, 78–80].

6.2 Experiment

We analyze thin films [70] of SmNiO$_3$ (SNO) and NdNiO$_3$ (NNO) on LaAlO$_3$ (LAO) and NdGaO$_3$ (NGO) substrates, labeled SNO/LAO-001, NNO /NGO-101 and NNO/NGO-110 using orthorhombic notation for NGO. These samples have $T_{MI} \sim 380$, 318 and 180 K respectively. The optical conductivity (Fig. 6.1) was measured as described in Ref. [57]; NNO/NGO-101 was remeasured to improve signal-to-noise. The metal insulator transition is revealed in the optical conductivity as the loss of the zero-frequency mode and the appearance of the peaks at 0.6 eV (peak A) and 1.3 eV (peak B).

To highlight the temperature dependence through T_{MI} and T_N we show in Fig. 6.2 the temperature dependence of the optical conductivities of SNO/LAO-001 and NNO/NGO-101 for selected photon energies.

Also shown are color plots of $d\sigma_1(\omega, T)/dT$ in the frequency-temperature plane. Most clearly visible in these data is the metal-insulator transition at T_{MI}. However, for some of the photon energies there is a soft step at temperatures T_i close to the Néel temperature ($T_N = 240K$ for NNO/NGO-101 and 210 K for SNO/LAO-001) (highlighted by arrows in Fig. 6.2). The softness of these steps is an important feature helping us to understand better the nature of the coupling between charge order and AF order, to which we will return below. For now we notice that the strength of the steps of $\sigma_1(\omega, T)$ around T_i seems to correlate with peaks A and B. In $d\sigma_1(\omega, T)/dT$ this shows up as the maxima at T_i for peak A and peak B.

We are interested in the additional conductivity spectrum, $\sigma_A(\omega)$, arising from the AF order. Leaving the softness of the step at T_i for discussion later in this article, we fitted for each photon energy a polynomial of the form $s_0^{\pm} + s_1^{\pm}(T - T_i) + s_2^{\pm}(T - T_i)^2$ to $\sigma_1(\omega, T)$ in a broad temperature range (about 100 K) above (+) and below (−) the inflection point T_i. The quantity $\sigma_A(\omega) = [s_1^+(\omega) - s_1^-(\omega)]T_i/2$ then represents, apart from a factor of order one, the additional conductivity spectrum extrapolated to zero temperature. The results of this analysis are shown in the bottom panel of Fig. 6.2. We see, that this corresponds to a reinforcement of the double peak structure already present in the PM insulating phase.

We now turn to an experimental observation that is of crucial importance for the subsequent discussion. As pointed out in the introduction, we can directly associate peaks A and B with spectral features reflecting the CO state, which are absent in the metal phase. The extra spectral weight in the two peaks as the temperature is lowered below T_N indicates that the charge ordering is enhanced by the AF order. We moreover see, that the effect of AF order is by and large limited to an increase of the intensity of peaks A and B. The intensity at or near the peak position, is therefore a measure of the order parameter Φ characterizing the charge order. More precisely, since the optical spectra and free energy are insensitive to the sign of Φ, we associate this intensity, apart from a temperature independent background contribution, to Φ^2. To analyze what happens at T_N we follow a phenomenological approach employing the
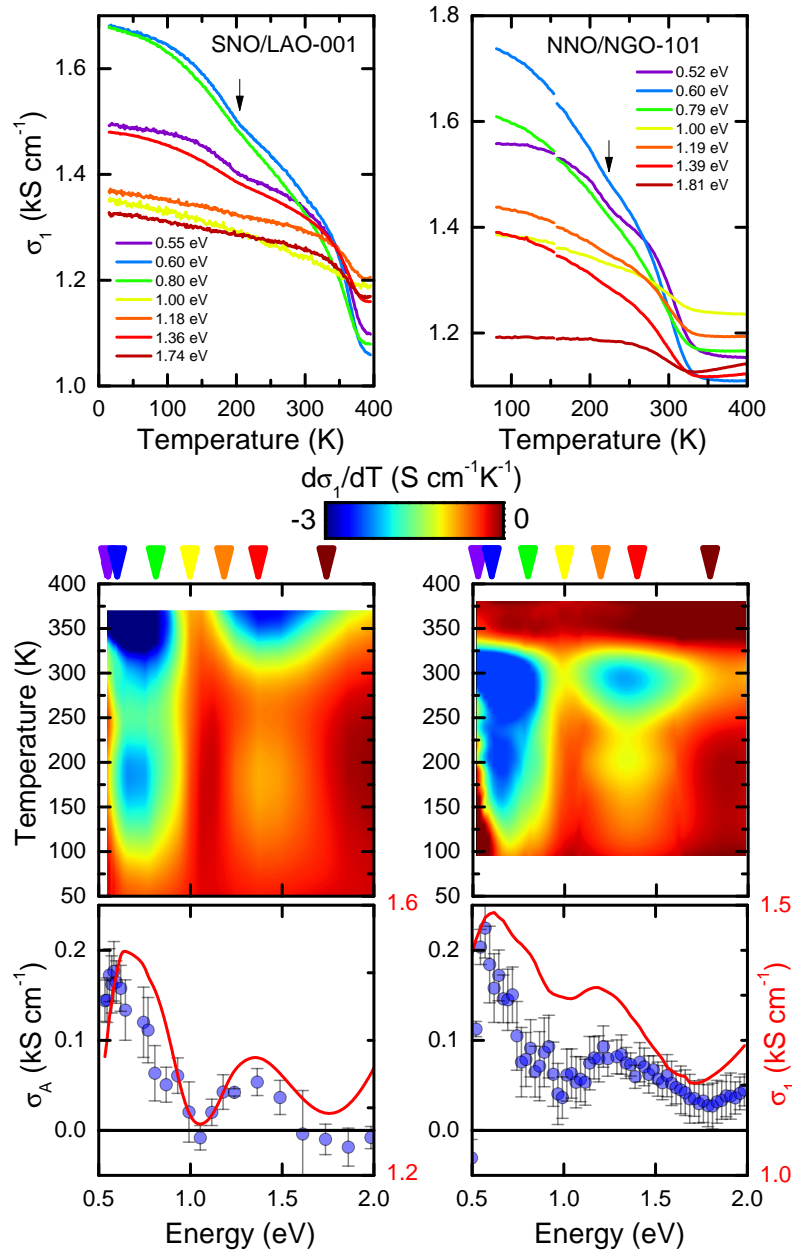
Figure 6.2: Temperature dependence of the optical conductivity, $\sigma_1(\omega, T)$, at selected photon energies for (top left) SNO/LAO-001 and (top right) NNO/NGO-101. The small jump at 150 K in the NNO/NGO-101 data is an experimental artifact and is ignored in the discussion. Middle panels: color plots of $d\sigma_1(\omega, T)/dT$. Bottom panels: The optical conductivity spectra at the Néel temperature, $\sigma_1(\omega, T_N)$ (red curves), and the antiferromagnetism induced contribution to the optical conductivity, $\sigma_A(\omega)$ (blue circles).

Landau theory of phase transitions, where the antiferromagnetism is characterized by the order parameter m. The free energy is an even function of both m and Φ, and can be expanded as

follows [1] [54, 81]

$$f = a\Phi^2 + \frac{b}{2!}\Phi^4 + \frac{c}{3!}\Phi^6 + \lambda\Phi^2 m^2 + \alpha m^2 + \frac{\beta}{2!}m^4 \qquad (6.1)$$

While a secondary role of charge order has been realized in a $PrNiO_3/PrAlO_3$ superlattice under compressive strain [82], the generic behavior of the nickelates is, that no antiferromagnetism occurs in the metal phase. This indicates that charge order is necessary for the antiferromagnetism to occur, implying that $\alpha = 0$. We will assume that the main temperature dependence close to the magnetic and metal-insulator transitions enters through a and λ

$$
\begin{aligned}
a(T) &= a_0\left([T/T_{MI}]^\eta - 1\right) \\
\lambda(T) &= \lambda_0\left([T/T_N]^\eta - 1\right)
\end{aligned}
\qquad (6.2)
$$

The AF and charge order parameters $m(T)$ and $\Phi(T)$ saturate at low temperatures, which we qualitatively describe by $\eta = 4$ (the precise value of η is not essential to our arguments). Below the temperatures T_{MI} (T_N) the coefficient a (λ) becomes negative. T_{MI} and T_N are materials parameters that depend on the tolerance factor t, for which we will use the phenomenological parameterization

$$
\begin{aligned}
T_N(t) &= \theta_N(t - t_N) \\
T_{MI}(t) &= \theta_{MI}(t_{MI}^+ - t)(t - t_{MI}^-)
\end{aligned}
\qquad (6.3)
$$

with the parameters given in Table 6.1. Since we are not interested in the absolute values of m, Φ and f, we choose the scale of these quantities such as to provide $c = \beta = a_0 = 1$. This leaves b and λ_0 as the only adjustable coefficients of our model. Finally we note, that several experiments indicate that for large values of the tolerance factor there is a single first order transition, whereas at least in part of the phase diagram where there are two phase transitions, the AF transition is second order and the metal-insulator transition weakly first order. The latter could indicate that the metal-insulator transition is *a priori* second order, while driven first order by coupling to the lattice. The splitting of a single first order transition into a set of second order transitions requires that $b = 0$, a fine tuning that is unlikely to occur by chance. Since several experiments have indicated first order behaviour at T_{MI} for most, if not all, values of the tolerance factor, we will choose $b = -0.25$ for the coefficient associated to CO, and $\lambda_0 = 0.8$ for the $\Phi^2 m^2$ coupling. The negative value of the parameter b (implying a first order transition at T_{MI} everywhere in the phase diagram) is to be understood as a consequence of the positive feedback of the electron-lattice coupling on the charge order. As we will see, this choice of

---

[1] In Ref. [81] a complex SDW order parameter $\psi = me^{i\theta}$ was introduced, leading to θ-dependent terms in the free energy containing odd powers of Φ : $f = v\Phi m^2 \cos 2\theta + um^4 \cos 4\theta + \dots$. When evaluated at its minimum with respect to θ this leads to an even function of Φ which is independent of m, and the next leading coupling between m and Φ allowed by symmetry is of the form $\Phi^2 m^2$.
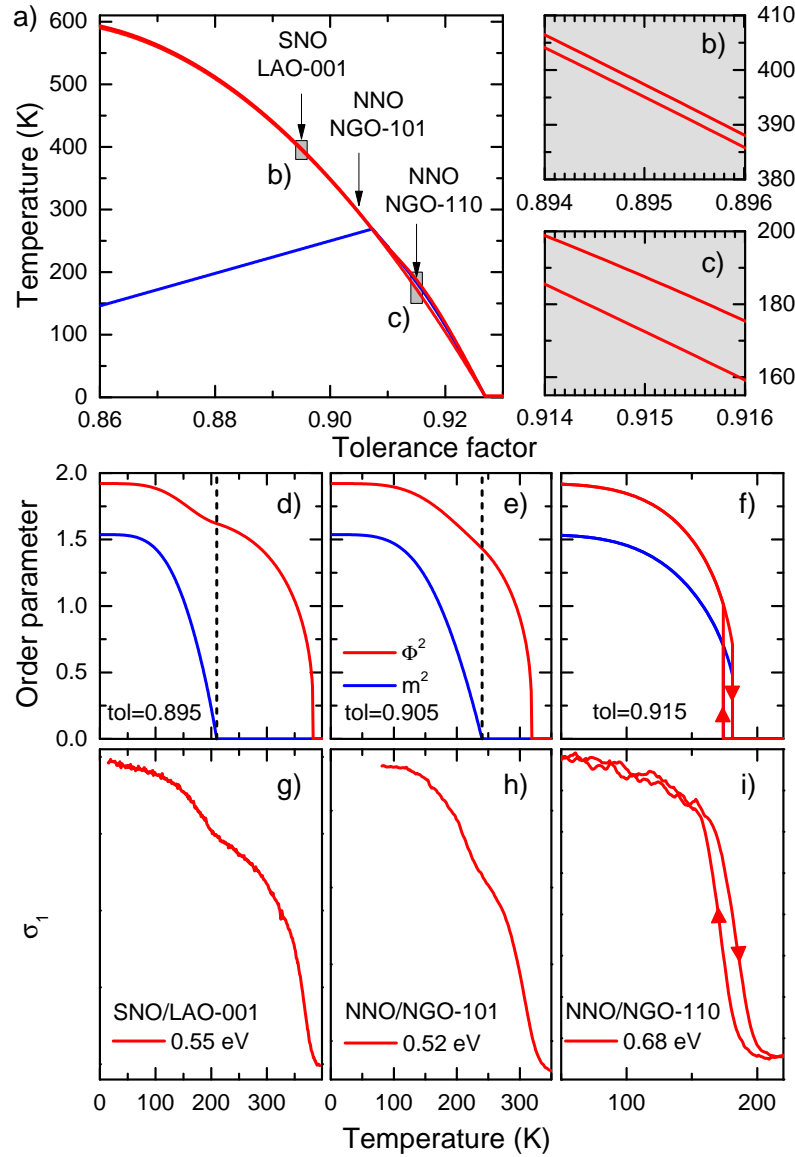
Figure 6.3: a) Calculated phase diagram in the temperature / tolerance factor plane of RNiO$_3$. Hysteresis limit curves enlargement centered on SNO/LAO-001 and on NNO/NGO-110 are shown in b) and c) respectively. d-f) Temperature dependence of the AF (m^2) and metal insulator (Φ^2) order parameters for three selected values of the tolerance factor, such as to match the Néel temperature and metal-insulator transition temperatures observed in the temperature dependence of the optical conductivity at the maximum of peak A of g) SNO/LAO-001, h) NNO/NGO-101 and i) NNO/NGO-110.

parameters illustrates qualitatively several thermodynamic aspects of these materials, including the temperature dependence of the optical experiments reported in the present manuscript.

a_0	b	c	λ_0	α	β
1	-0.25	1	0.8	0	1
θ_N (K)	t_N	θ_{MI} (K)	t_{MI}^+	t_{MI}^-	η
2597	0.804	101198	0.927	0.773	4

Table 6.1: Parameters used for the calculations in Figs. 6.3 and 6.5.

The phase diagram in the tolerance factor / temperature plane can now be reproduced with the help of the parameters described above and with Eq. 6.1. The result is displayed in Fig. 6.3a). In the region of hysteresis the free energy has a metastable minimum coexisting with the stable one. Interestingly the phase diagram shows a widening of this region around $t = 0.915$ for the following reason: The free energy (Eq. 6.1) at its minimum with respect to m equals

$$
\begin{aligned}
f &= a\Phi^2 + \frac{\tilde{b}}{2!}\Phi^4 + \frac{c}{3!}\Phi^6 \\
\tilde{b} &= b - \lambda^2 \ (T < T_N) \quad ; \quad \tilde{b} = b \ (T > T_N)
\end{aligned}
\tag{6.4}
$$

Since a first order transition requires a negative value of the coefficient $\tilde{b}$, the $-\lambda^2$ contribution to $\tilde{b}$ enhances the first order character and the size of the hysteresis loop around T_{MI}, and this can only happen when $T_N > T_{MI}$. The hysteresis of about 15 K is close to the behavior observed in the bulk compound $NdNiO_3$ (and sample NNO/NGO-110). Such hysteresis is also present in the optical spectra, shown in Fig. 6.4 for the original ellipsometric parameters Ψ and Δ from which the optical conductivity was obtained using the method described in Ref. [57]. Since these thermal cycles take several hours, the small differences observed in SNO/LAO-001 and NNO/NGO-101 during heating and cooling may be partly or entirely caused by instrument drift or absorption and desorption of a small quantity of gas molecules at the sample surface.

In the middle panels of Fig. 6.3 the temperature dependence of Φ^2 and m^2 calculated for $t = 0.895$ (SNO/LAO-001, Fig. 6.3b), $t = 0.905$ (NNO/NGO-101, Fig. 6.3c), and $t = 0.915$ (NNO/NGO-110, Fig. 6.3d) is shown. While for all cases the calculation shows that the transition at T_{MI} is first order, the hysteresis of the two formers are too small to display on this scale whereas, for the latter, the hysteresis is about 10 K, and shows clearly in the temperature dependence. The experimental data of the optical conductivity at an energy close to peak A, shown in Fig. 6.3e-g, closely follow these trends.

We now turn our attention to the details of the temperature dependence close to T_N. If the intensity of peaks A and B were to track the antiferromagnetic order, a kink would be expected at T_N. The experimental data in the top panel of Fig. 6.2 and bottom panel of Fig. 6.3 show only an inflexion point, not a kink. In principle it is not unusual that some broadening occurs, for
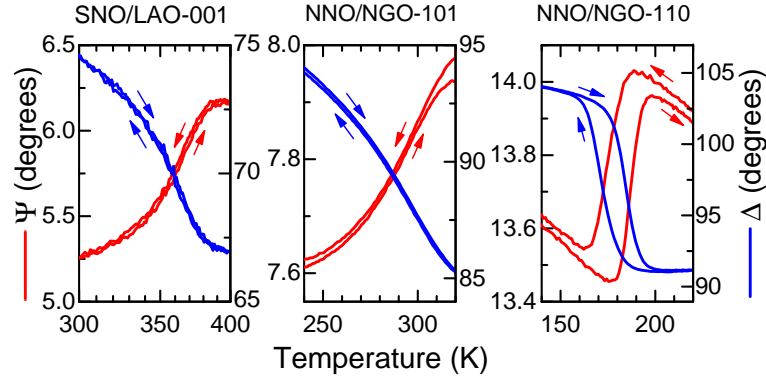
Figure 6.4: Temperature dependence of the ellipsometric parameters of the three samples, showing strong hysteresis for NNO/NGO-110 (right panel), and absence of hysteresis for NNO/NGO-101 (central panel) and SNO/LAO-001 (left panel). Red curves are during warm-up, blue curves during cool-down.

example if T_N would not be completely homogeneous across the area of the sample. The kink in $\sigma_1(\omega, T)$ would then be replaced by an inflection point, and one would be tempted to associate the average Néel temperature with this inflection point. However, the phenomenological Landau modeling tells a different story: Minimizing $f(\Phi, m)$ (Eq. 6.1, $c = \beta = 1$) with respect to Φ and m and eliminating λ, leads to the following relation between the equilibrium values of Φ^2 and m^2

$$\Phi^2 = -b \pm \sqrt{b^2 - 2a + 2m^4/\Phi^2} \tag{6.5}$$

Deep inside the insulating state and close to T_N we can expand the right hand side in m^4/Φ^2. The leading order of this expansion is proportional to m^4, which close to the transition is proportional to $(T_N - T)^2$. This soft onset of the AF-induced contribution to Φ^2 is a direct consequence of setting $\alpha = 0$, so that the (remaining) m^2 term in the free energy expression is proportional to the charge order parameter Φ^2, in other words that charge order is a *conditio sine qua non* for the occurence of AF order (at least of the type that we are considering here). In particular it implies that the temperature derivative $d\Phi^2/dT$ should have a kink at T_N as shown in the top panel of Fig. 6.5. Comparing this to the temperature derivative of the experimental optical conductivity at energies close to peaks A and B of samples SNO/LAO-001 and NNO/NGO-101 (bottom panel of the same figure) we conclude that, with the parameters $\lambda_0 = 0.8$, $b = -0.25$, and $\alpha = 0$ the temperature trend of the SW and its behaviour at the phase transitions, is very well described by the Landau-theory. The requirement that $\alpha = 0$ corroborates another experimental observation, namely that these compounds are paramagnetic in the metal phase. Note also that, as a result of the soft onset, the inflection point in the $\Phi^2(T)$ curve occurs well below the actual T_N.
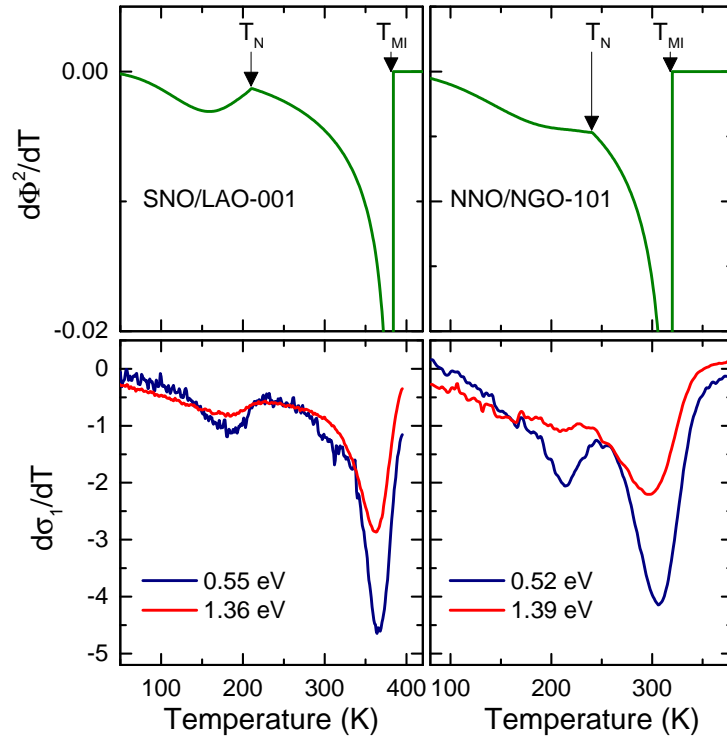
58

Figure 6.5: Temperature derivative of the charge order parameter Φ^2 (top panels) and the temperature derivative of the optical conductivities of SNO/LAO-001 and NNO/NGO-101 (bottom panels) measured at photon energies corresponding to the maximum of peaks A (navy) and B (red).

6.3 Conclusions

We observed a significant impact of antiferromagnetic (AF) order on the optical conductivity spectrum of $RNiO_3$. The intensity of two prominent conductivity peaks was previously demonstrated to track the charge order (CO) accompanied by bond disproportionation in these compounds [57]. We now observe that in the antiferromagnetic state an additional spectral weight is added, proportional to m^4 where m is the antiferromagnetic order parameter. This soft onset of the AF-related spectral weight proves that the charge order is a *conditio sine qua non* for the AF order, and is excellently described by a Landau model for the free energy with two coupled (CO and AF) order parameters. The temperature dependence upon thermal cycling indicates that the transition into a simultaneously charge and AF ordered phase, has much stronger hysteresis than the transition into a charge ordered phase without AF order. This aspect is also very well described by the aforementioned Landau model. These observations and conclusions permit to describe a wealth of transport and spectroscopic data in a unified thermodynamic framework, using a small set of Landau parameters that may serve as a basis of future microscopic models.

Appendices

Appendix A

Fresnel Equations

A.1 Mathematical derivation

Full derivation of Fresnel equation. After [83]

A.2 s and p polarized light reflection

The interface imposes boundary conditions. At the interface, the electric field vector in both medium must be equal (in direction and amplitude). For the p-polarization, we can write:

$$E_i^p cos\theta_i - E_r^p cos\theta_r = E_t^p cos\theta_t$$
$$B_i^p + B_r^p = B_t^p$$

with $E = \frac{c}{n}B$ we can write eq.nbr as

$$E_i^p \frac{n_i}{c} + E_r^p \frac{n_i}{c} = E_t^p \frac{n_t}{c}$$
$$E_t^p = \frac{n_i}{n_t}(E_i^p + E_r^p)$$

Substituting E_t^p in eq.nbr, we have:

$$E_i^p \cos\theta_i - E_r^p \cos\theta_r = \frac{n_i}{n_t} E_i^p \cos\theta_t + \frac{n_i}{n_t} E_r^p \cos\theta_t$$

$$E_i^p \left(\cos\theta_i - \frac{n_i}{n_t} \cos\theta_t\right) = E_r^p \left(\cos\theta_r + \frac{n_i}{n_t} \cos\theta_t\right)$$

$$r_p = \frac{E_r^p}{E_i^p} = \frac{\cos\theta_i - \frac{n_i}{n_t} \cos\theta_t}{\cos\theta_r - \frac{n_i}{n_t} \cos\theta_t}$$

$$r_p = \frac{n_t \cos\theta_i - n_i \cos\theta_t}{n_t \cos\theta_i + n_i \cos\theta_t}$$

Similar arguments hold for $r_s = \frac{E_r^s}{E_i^s}$.

A.3 Phase Factor

We define the propagation number $K = \frac{2\pi}{\lambda}$. It represents the phase change per unit length along the optical path. In a medium of refractiv index n we write $K = \frac{2\pi}{\lambda} n$. The phase difference between the two beam $\Delta\Phi$ is:

$$\Delta\Phi = \Delta\Phi_{AC} - \Delta\Phi_{AD}$$

$$\Delta\Phi_{AC} = K\overline{AB} + K\overline{BC}$$

$$\Delta\Phi_{AD} = K\overline{AD}$$

$$\overline{AB} = \overline{BC} = d\frac{1}{cos\theta_1}$$

$$\overline{AD} = \overline{AC}sin\theta_0$$

$$\overline{AC} = 2d \cdot tg\,\theta_1$$

$$\overline{AD} = 2d \cdot tg\,\theta_1 \cdot sin\theta_0$$

$$sin\theta_0 = \frac{n_1}{n_0}sin\theta_1 \;(Snell\;law)$$

$$tg\theta = \frac{sin\theta}{cos\theta}$$

$$\overline{AD} = 2d\frac{n_1}{n_0}\frac{sin\theta_1{}^2}{cos\theta_1}$$

$$\Delta\Phi_{AC} = K \cdot 2 \cdot d\frac{1}{cos\theta_1} = \frac{4\pi dn_1}{\lambda cos\theta_1}$$

$$\Delta\Phi_{AD} = \frac{2\pi n_0}{\lambda} \cdot 2d\frac{n_1}{n_0}\frac{sin\theta_1{}^2}{cos\theta_1} = \frac{4\pi dn_1}{\lambda cos\theta_1} \cdot sin\theta_1{}^2$$

$$\Delta\Phi = \frac{4\pi dn_1}{\lambda cos\theta_1}\left(1 - sin\theta_1{}^2\right)$$

$$= \frac{4\pi dn_1}{\lambda cos\theta_1}cos\theta_1{}^2$$

$$= \frac{4\pi dn_1}{\lambda} \cdot cos\theta_1$$

A.4   Total Reflectivities

$$r_{012} = r_{01} + t_{01}t_{10}r_{12}e^{-2i\beta} + t_{01}t_{10}r_{10}r_{12}^2e^{-4i\beta} + ...$$

This is an infinit serie of the form $y = a + ar + ar^2 + ar^3 + ...$ that can be reduce to $y = a\frac{1}{1-r}$. Writing

$$a = t_{01}t_{10}r_{12}e^{-2i\beta}$$

$$b = r_{10}r_{12}e^{-2i\beta}$$

we have

$$r_{012} = r_{01} + \frac{t_{10}r_{12}e^{-2i\beta}}{1 - r_{10}r_{12}e^{-2i\beta}}$$

with

$$r_{10} = -r_{01}$$
$$t_{01}t_{10} = 1 - r_{01}^2$$

we can write

$$\begin{aligned} r_{012} &= r_{01} + \frac{(1 - r_{01}^2)r_{12}e^{-2i\beta}}{1 + r_{10}r_{12}e^{-2i\beta}} \\ &= \frac{r_{01} + r_{01}^2 r_{12}e^{-2i\beta} + (1 - r_{01}^2)r_{12}e^{-2i\beta}}{1 + r_{10}r_{12}e^{-2i\beta}} \\ &= \frac{r_{01} + r_{01}^2 r_{12}e^{-2i\beta} + r_{12}e^{-2i\beta} - r_{01}^2 r_{12}e^{-2i\beta}}{1 + r_{10}r_{12}e^{-2i\beta}} \\ &= \frac{r_{01} + r_{12}e^{-2i\beta}}{1 + r_{01}r_{12}e^{-2i\beta}} \end{aligned}$$

To summarize, for s- and p-polarized light we have:

$$r_{012}^s = \frac{r_{01}^s + r_{12}^s e^{-2i\beta}}{1 + r_{01}^s r_{12}^s e^{-2i\beta}} \qquad r_{012}^p = \frac{r_{01}^p + r_{12}^p e^{-2i\beta}}{1 + r_{01}^p r_{12}^p e^{-2i\beta}}$$

$$r_{jk}^s = \frac{N_j \cos\theta_j - N_k \cos\theta_k}{N_j \cos\theta_j + N_k \cos\theta_k} \qquad r_{jk}^p = \frac{N_k \cos\theta_j - N_j \cos\theta_k}{N_k \cos\theta_j + N_j \cos\theta_k}$$

$$\beta = \frac{1}{2}\Delta\Phi = \frac{2\pi d n_1}{\lambda} \cdot \cos\theta_1$$

A.5 Numerical Inversion

```
#!/usr/bin/python2.7
```

```python
#
# Arguments number 1 and 2 are Substrate Eps1 and Eps2
# Arguments number 3 and 4 are Film-Subst Psi and Delta
# Arguments number 5 and 6 are Initial guess for film Eps1 and Eps2
# Arguments number 7 and 8 are Incident angle and film thinckness
# Argument number 9 is whether or not to display Rho at the end of the fit
#
# Related jupyter notebook is: PhdData/NoteBook/2017.07.30-Plot-Fresnel-Equations.ipynb
#
# Summary in PhdData/Documents/2015.02.19-ComplexFitting
#
# Should check if all provided input file have the same length
#
# Laste edited 2017.07.31
# julien.ruppen@gmail.com
#

import os
import sys
import numpy as np
import matplotlib.pyplot as plt
from lmfit import minimize, Minimizer, Parameters, report_fit


IncAngle = sys.argv[7]
FlmThick = sys.argv[8]


PlotRho = sys.argv[9]


def RefractIndex(Eps1,Eps2):
    n = ( ((Eps1**2 + Eps2**2)**(0.5) + Eps1 ) / 2 )**(0.5)
    k = ( ((Eps1**2 + Eps2**2)**(0.5) - Eps1 ) / 2 )**(0.5)
    return n,k


def DielecCste(n,k):
    e1 = n**2 - k**2
    e2 = 2*n*k
    return e1,e2


# Initial guess for film diel. cste
TmpFilmEps1 = np.loadtxt(sys.argv[5])
TmpFilmEps2 = np.loadtxt(sys.argv[6])
FilmEps1 = TmpFilmEps1[:,1]#+0.0
FilmEps2 = TmpFilmEps2[:,1]#+0.0
#----------------------------------------------------------
AllReffit_n1= RefractIndex(FilmEps1,FilmEps2)[0]
```

A. FRESNEL EQUATIONS

```python
AllReffit_k1= RefractIndex(FilmEps1,FilmEps2)[1]
#------------------------------------------------------------

# Bulk Substrate Eps1 and Eps2
TmpSubstEps1 = np.loadtxt(sys.argv[1])
TmpSubstEps2 = np.loadtxt(sys.argv[2])
SubstEps1 = TmpSubstEps1[:,1]
SubstEps2 = TmpSubstEps2[:,1]
#------------------------------------------------------------
AllExp_n2 = RefractIndex(SubstEps1,SubstEps2)[0]
AllExp_k2 = RefractIndex(SubstEps1,SubstEps2)[1]
#------------------------------------------------------------

# Film-Substrate PSI and DELTA
TmpPsi   = np.loadtxt(sys.argv[3])
TmpDelta = np.loadtxt(sys.argv[4])
ExpPsi   = TmpPsi[:,1] * np.pi/180
ExpDelta = TmpDelta[:,1] * np.pi/180
#------------------------------------------------------------
AllExpRho = np.tan(ExpPsi) * np.exp(1j*(ExpDelta))
#------------------------------------------------------------


# WaveNumber
WveNbr=TmpPsi[:,0]
#------------------------------------------------------------
All_WL = 1/WveNbr   # in cm
#------------------------------------------------------------

def SetSystemCst(inc_angle,flm_thick):

    global phi0,thick1
    phi0 = np.float(inc_angle)*np.pi/180
    thick1 = np.float(flm_thick) #(cm)

    # Air refractive index
    global n0,k0
    n0=1
    k0=0

def SetSystemVar(Idx):

    global ExpRho
    ExpRho = AllExpRho[Idx]
```

```python
    global n2,k2
    n2 = AllExp_n2[Idx]
    k2 = AllExp_k2[Idx]

    global wl
    wl = All_WL[Idx]

global Param_n1, Param_k1
Param_n1 = Parameters()
Param_k1 = Parameters()


def Set_n1(Input_n1):
    global n1
    n1 = Input_n1
    Param_n1.add('n1', value=n1)


def Set_k1(Input_k1):
    global k1
    k1 = Input_k1
    Param_k1.add('k1', value=k1)


# THESE ARE THE FRESNEL EQUATIONS FOR A THIN FILM ON A BULK SUBSTRATE
def phi1(n1):
    phi1 = np.arcsin(n0/n1 * np.sin(phi0))
    return phi1


def phi2(n1):
    phi2 = np.arcsin(n1/n2 * np.sin(phi1(n1)))
    return phi2


def r1s(n1,k1):
    a = n0*np.cos(phi0)
    b = (n1+k1*1j)*np.cos(phi1(n1))
    Reflect1s = (a - b) / (a + b)
    return Reflect1s


def r1p(n1,k1):
    a = n0*np.cos(phi1(n1))
    b = (n1+k1*1j)*np.cos(phi0)
    Reflect1p = (a - b) / (a + b)
    return Reflect1p


def r2s(n1,k1):
    a = (n1+k1*1j)*np.cos(phi1(n1))
    b = (n2+k2*1j)*np.cos(phi2(n1))
```

```python
    Reflect2s = (a - b) / (a + b)
    return Reflect2s


def r2p(n1,k1):
    a = (n1+k1*1j)*np.cos(phi2(n1))
    b = (n2+k2*1j)*np.cos(phi1(n1))
    Reflect2p = (a - b) / (a + b)
    return Reflect2p


# wavelength (wl) and thickness of layer 1 (thick1) must have the same unit
def delt1(n1,k1):
    delta1 = 2*np.pi*(n1+k1*1j)*thick1*np.cos(phi1(n1))/wl
    return -delta1


# two interface reflection
def ReflectS(n1,k1):
    Rs = (r1s(n1,k1) + r2s(n1,k1)*np.exp(-2*1j*delt1(n1,k1))) \\
    / (1 + r1s(n1,k1)*r2s(n1,k1)*np.exp(-2*1j*delt1(n1,k1)))
    return Rs


# two interface reflection
def ReflectP(n1,k1):
    Rp = (r1p(n1,k1) + r2p(n1,k1)*np.exp(-2*1j*delt1(n1,k1))) \\
    / (1 + r1p(n1,k1)*r2p(n1,k1)*np.exp(-2*1j*delt1(n1,k1)))
    return Rp


def CalcRho(n1,k1):
    rho = ReflectP(n1,k1) / ReflectS(n1,k1)
    return rho


# This is the objective function
def Fit_n1(Initn1):

    In1 = Initn1['n1'].value
    diff =  CalcRho(In1,k1) - ExpRho
    return diff.real**2 + diff.imag**2


def Fit_k1(Initk1):

    Ik1 = Initk1['k1'].value
    diff =  CalcRho(n1,Ik1) - ExpRho
    return diff.real**2 + diff.imag**2


MinMethod = 'leastsq'
PrintInfo = 1
```

```python
NIterRI = 3

IndexMin = 0
IndexMax = len(WveNbr)

SetSystemCst(IncAngle,FlmThick)

SpecLen = IndexMax - IndexMin
Alln1=np.zeros((SpecLen))
Allk1=np.zeros((SpecLen))

CalcRho_Reffit = np.zeros((SpecLen),dtype=complex)
CalcRho_FromFt = np.zeros((SpecLen),dtype=complex)

Set_n1(AllReffit_n1[IndexMin])
Set_k1(AllReffit_k1[IndexMin])

for i in range(SpecLen):

    Idx = IndexMin + i

    SetSystemVar(Idx)

    CalcRho_Reffit[i] = CalcRho(AllReffit_n1[Idx],AllReffit_k1[Idx])

    # Here the number of iteration from real to imag N for a single freq
    for l in range(NIterRI):

        CC = Minimizer(Fit_k1,Param_k1,nan_policy='omit')
        DD = CC.minimize(method=MinMethod)

        k1 = DD.params['k1'].value
        Set_k1(k1)

        AA = Minimizer(Fit_n1,Param_n1,nan_policy='omit')
        BB = AA.minimize(method=MinMethod)

        n1 = BB.params['n1'].value
        Set_n1(n1)

        Alln1[i] = BB.params['n1'].value
        Allk1[i] = DD.params['k1'].value

    CalcRho_FromFt[i] = CalcRho(n1,k1)
```

```python
    if (PrintInfo):
        print "Index: ", IndexMin+i, " WaveNbr: ", np.int(WveNbr[IndexMin+i])
        print BB.message, "Fit_n1 ChiSqrt: ", BB.chisqr
        print DD.message, "Fit_k1 ChiSqrt: ", DD.chisqr

Output_e1 = np.zeros((len(Alln1),2))
Output_e2 = np.zeros((len(Alln1),2))
Output_e1[:,0] = WveNbr
Output_e2[:,0] = WveNbr
Output_e1[:,1] = DielecCste(Alln1,Allk1)[0]
Output_e2[:,1] = DielecCste(Alln1,Allk1)[1]

FittedFilm_e1 = "FittedFilm.Eps1.txt"
FittedFilm_e2 = "FittedFilm.Eps2.txt"

np.savetxt(FittedFilm_e1,Output_e1,fmt="%8.10e")
np.savetxt(FittedFilm_e2,Output_e2,fmt="%8.10e")
```

Bibliography

[1] G. A. Sawatzky and J. W. Allen, "Magnitude and origin of the band gap in NiO," *Physical Review Letters*, vol. 53, pp. 2339–2342, 1984.

[2] A. Sleight, J. Gillson, and P. Bierstedt, "High-temperature superconductivity in the $BaPb_{1-x}Bi_xO_3$ systems," *Solid State Communications*, vol. 17, no. 1, pp. 27 – 28, 1975.

[3] G. Demazeau, A. Marbeuf, M. Pouchard, and P. Hagenmuller, "Sur une serie de composes oxygenes du nickel trivalent derives de la perovskite," *Journal of Solid State Chemistry*, vol. 3, no. 4, pp. 582–589, 1971.

[4] P. Lacorre, J. B. Torrance, J. Pannetier, A. I. Nazzal, P. W. Wang, and T. C. Huang, "Synthesis, crystal structure, and properties of metallic $PrNiO_3$: Comparison with metallic $NdNiO_3$ and semiconducting $SmNiO_3$," *Journal of Solid State Chemistry*, vol. 91, no. 2, pp. 225–237, 1991.

[5] P. Laffez, M. Zaghrioui, R. Retoux, and P. Lacorre, "Oriented and polycrystalline $NdNiO_3$ thin films on silicon substrate," *Journal of Magnetism and Magnetic Materials*, vol. 211, no. 1, pp. 111–117, 2000.

[6] M. A. Novojilov, O. Y. Gorbenko, I. E. Graboy, A. R. Kaul, H. W. Zandbergen, N. A. Babushkina, and L. M. Belova, "Perovskite rare-earth nickelates in the thin-film epitaxial state," *Applied Physics Letters*, vol. 76, no. 15, pp. 2041–2043, 2000.

[7] F. Conchon, A. Boulle, C. Girardot, S. Pignard, R. Guinebretiere, E. Dooryhee, J.-L. Hodeau, F. Weiss, J. Kreisel, and J.-F. Berar, "Epitaxial stabilization of $SmNiO_3$ films on (0 0 1)$SrTiO_3$ substrates," *Journal of Physics D: Applied Physics*, vol. 40, no. 16.

[8] A. Tiwari, C. Jin, and J. Narayan, "Strain induced tuning of metal insulator transition in $NdNiO_3$," *Applied Physics Letters*, vol. 80, no. 21, p. 4039, 2002.

[9] R. Scherwitzl, "Metal-insulator transitions in nickelate heterostructures," Ph.D. dissertation, University of Geneva, 2012.

[10] J. L. García-Muñoz, J. Rodríguez-Carvajal, P. Lacorre, and J. B. Torrance, "Neutron-diffraction study of RNiO$_3$ (R=La,Pr,Nd,Sm): Electronically induced structural changes across the metal-insulator transition," *Phys. Rev. B*, vol. 46, pp. 4414–4425, 1992.

[11] P. Lacorre, J. Torrance, J. Pannetier, A. Nazzal, P. Wang, and T. Huang, "Synthesis, crystal structure, and properties of metallic PrNiO3: Comparison with metallic NdNiO3 and semiconducting SmNiO3," *Journal of Solid State Chemistry*, vol. 91, no. 2, pp. 225–237, Apr 1991.

[12] M. Dressel and G. Grüner, *Electrodynamics of Solids: Optical Properties of Electrons in Matter*, 1st ed. Cambridge: Cambridge University Press, 2002.

[13] H. Fujiwara, *Spectroscopic Ellipsometry: Principles and Applications*, 1st ed. Chichester, England ; Hoboken, NJ: Wiley, 2007.

[14] H. Tompkins and E. A. Irene, *Handbook of Ellipsometry*, 1st ed. Norwich, NY : Heidelberg, Germany: William Andrew, 2006.

[15] M. Newville, T. Stensitzki, D. B. Allen, and A. Ingargiola, "Lmfit: Non-linear least-square minimization and curve-fitting for python," 2014.

[16] M. Gilliot, "Extraction of complex refractive index of absorbing films from ellipsometry measurement," *Thin Solid Films*, vol. 520, no. 17, pp. 5568 – 5574, 2012.

[17] K. Terakura, A. R. Williams, T. Oguchi, and J. Kübler, "Transition-metal monoxides: Band or mott insulators," *Phys. Rev. Lett.*, vol. 52, pp. 1830–1833, May 1984.

[18] A. Fujimori and F. Minami, "Valence-band photoemission and optical absorption in nickel compounds," *Phys. Rev. B*, vol. 30, pp. 957–971, Jul 1984.

[19] N. F. Mott, "The basis of the electron theory of metals, with special reference to the transition metals," *Proceedings of the Physical Society. Section A*, vol. 62, no. 7, p. 416, 1949.

[20] J. Hubbard, "Electron correlations in narrow energy bands," *Proceedings of the Royal Society of London A: Mathematical, Physical and Engineering Sciences*, vol. 276, no. 1365, pp. 238–257, 1963.

[21] S. Ciuchi and S. Fratini, "Signatures of polaronic charge ordering in optical and dc conductivity using dynamical mean field theory," *Phys. Rev. B*, vol. 77, p. 205127, May 2008.

[22] D. Sarma, "Electronic structure of transition metal compounds: Photoemission experiments and model hamiltonian calculations," *Journal of Solid State Chemistry*, vol. 88, no. 1, pp. 45 – 52, 1990.

[23] T. Mizokawa, H. Namatame, A. Fujimori, K. Akeyama, H. Kondoh, H. Kuroda, and N. Kosugi, "Origin of the band gap in the negative charge-transfer-energy compound $NaCuO_2$," *Phys. Rev. Lett.*, vol. 67, no. 12, pp. 1638–1641, 1991.

[24] J. Zaanen, G. A. Sawatzky, and J. W. Allen, "Band gaps and electronic structure of transition-metal compounds," *Phys. Rev. Lett.*, vol. 55, no. 4, pp. 418–421, 1985.

[25] S. Johnston, A. Mukherjee, I. Elfimov, M. Berciu, and G. A. Sawatzky, "Charge disproportionation without charge transfer in the rare-earth-element nickelates as a possible mechanism for the metal-insulator transition," *Phys. Rev. Lett.*, vol. 112, p. 106404, 2014.

[26] J. A. Alonso, J. L. Garcia Munoz, M. T. Fernandez Diaz, M. A. G. Aranda, M. J. Martinez Lope, and M. T. Casais, "Charge disproportionation in $RNiO_3$ perovskites: Simultaneous metal-insulator and structural transition in $YNiO_3$," *Phys. Rev. Lett.*, vol. 82, no. 19, pp. 3871–3874, 1999.

[27] J. A. Alonso, M. J. Martínez-Lope, I. A. Presniakov, A. V. Sobolev, V. S. Rusakov, A. M. Gapochka, G. Demazeau, and M. T. Fernández-Díaz, "Charge disproportionation in $RNiO_3$ (R= Tm, Yb) perovskites observed in situ by neutron diffraction and [57]Fe probe Mössbauer spectroscopy," *Phys. Rev. B*, vol. 87, no. 18, p. 184111, 2013.

[28] J. A. Alonso, M. J. Martinez-Lope, M. T. Casais, J. L. Garcia-Munoz, and M. T. Fernandez-Diaz, "Room-temperature monoclinic distortion due to charge disproportionation in $RNiO_3$ perovskites with small rare-earth cations (R=Ho, Y, Er, Tm, Yb, and Lu): A neutron diffraction study," *Phys. Rev. B*, vol. 61, no. 3, pp. 1756–1763, 2000.

[29] I. Presniakov, A. Baranov, G. Demazeau, V. Rusakov, A. Sobolev, J. A. Alonso, M. J. Martínez-Lope, and K. Pokholok, "Evidence through Mössbauer spectroscopy of two different states for [57]Fe probe atoms in $RNiO_3$ perovskites with intermediate-size rare earths, R = Sm, Eu, Gd, Dy," *J. Phys.: Condens. Matter*, vol. 19, no. 3, p. 036201, 2007.

[30] J. A. Alonso, M. J. Martínez-Lope, M. T. Casais, J. L. García-Muñoz, M. T. Fernández-Díaz, and M. A. G. Aranda, "High-temperature structural evolution of $RNiO_3$ (R=Ho, Y, Er, Lu) perovskites: Charge disproportionation and electronic localization," *Phys. Rev. B*, vol. 64, p. 094102, 2001.

[31] J. A. Alonso, M. J. Martínez-Lope, M. T. Casais, J. L. García-Muñoz, and M. T. Fernández-Díaz, "Room-temperature monoclinic distortion due to charge disproportionation in

RNiO$_3$ perovskites with small rare-earth cations (R=Ho, Y, Er, Tm, Yb, and Lu): A neutron diffraction study," *Phys. Rev. B*, vol. 61, pp. 1756–1763, 2000.

[32] C. Piamonteze, H. C. N. Tolentino, A. Y. Ramos, N. E. Massa, J. A. Alonso, M. J. Martínez-Lope, and M. T. Casais, "Short-range charge order in RNiO$_3$ perovskites (R=Pr, Nd, Eu, Y) probed by x-ray-absorption spectroscopy," *Phys. Rev. B*, vol. 71, p. 012104, 2005.

[33] M. L. Medarde, "Structural, magnetic and electronic properties of perovskites (R = Rare Earth)," *Journal of Physics: Condensed Matter*, vol. 9, no. 8, p. 1679, 1997.

[34] J. A. Alonso, J. L. García-Muñoz, M. T. Fernández-Díaz, M. A. G. Aranda, M. J. Martínez-Lope, and M. T. Casais, "Charge disproportionation in RNiO$_3$ perovskites: Simultaneous metal-insulator and structural transition in YNiO$_3$," *Phys. Rev. Lett.*, vol. 82, pp. 3871–3874, 1999.

[35] U. Staub, G. I. Meijer, F. Fauth, R. Allenspach, J. G. Bednorz, J. Karpinski, S. M. Kazakov, L. Paolasini, and F. d'Acapito, "Direct observation of charge order in an epitaxial NdNiO$_3$ film," *Phys. Rev. Lett.*, vol. 88, p. 126402, 2002.

[36] J. Rodríguez-Carvajal, S. Rosenkranz, M. Medarde, P. Lacorre, M. T. Fernandez-Díaz, F. Fauth, and V. Trounov, "Neutron-diffraction study of the magnetic and orbital ordering in ^{154}SmNiO$_3$ and ^{153}EuNiO$_3$," *Phys. Rev. B*, vol. 57, pp. 456–464, 1998.

[37] M. T. Fernández-Díaz, J. A. Alonso, M. J. Martínez-Lope, M. T. Casais, and J. L. García-Muñoz, "Magnetic structure of the HoNiO$_3$ perovskite," *Phys. Rev. B*, vol. 64, p. 144417, 2001.

[38] Y. Bodenthin, U. Staub, C. Piamonteze, M. García-Fernández, M. J. Martínez-Lope, and J. A. Alonso, "Magnetic and electronic properties of RNiO$_3$ (R = Pr, Nd, Eu, Ho and Y) perovskites studied by resonant soft x-ray magnetic powder diffraction," *Journal of Physics: Condensed Matter*, vol. 23, no. 3, p. 036002, 2011.

[39] T. Mizokawa, D. I. Khomskii, and G. A. Sawatzky, "Spin and charge ordering in self-doped mott insulators," *Phys. Rev. B*, vol. 61, pp. 11 263–11 266, 2000.

[40] H. Park, A. J. Millis, and C. A. Marianetti, "Site-selective mott transition in rare-earth-element nickelates," *Phys. Rev. Lett.*, vol. 109, p. 156402, 2012.

[41] M. K. Stewart, J. Liu, M. Kareev, J. Chakhalian, and D. N. Basov, "Mott physics near the insulator-to-metal transition in NdNiO$_3$," *Phys. Rev. Lett.*, vol. 107, p. 176401, 2011.

[42] A. Subedi, O. E. Peil, and A. Georges, "Low-energy description of the metal-insulator transition in the rare-earth nickelates," *Phys. Rev. B*, vol. 91, p. 075128, 2015.

[43] M. A. Anisimov, E. E. Gorodetskii, and V. M. Zaprudskii, "Phase transitions with coupled order parameters," *Soviet Physics Uspekhi*, vol. 24, no. 1, p. 57, 1981.

[44] T. Moriya and K. Usami, "Coexistence of ferro- and antiferromagnetism and phase transitions in itinerant electron systems," *Solid State Communications*, vol. 23, no. 12, pp. 935 – 938, 1977.

[45] S. Niziol, A. Zieba, R. Zach, M. Baj, and L. Dmowski, "Structural and magnetic phase transitions in $Co_xNi_{1-x}MnGe$ system under pressure," *Journal of Magnetism and Magnetic Materials*, vol. 38, no. 2, pp. 205 – 213, 1983.

[46] C. Girardot, J. Kreisel, S. Pignard, N. Caillault, and F. Weiss, "Raman scattering investigation across the magnetic and metal-insulator transition in rare earth nickelate $RNiO_3$ (R=Sm, Nd) thin films," *Phys. Rev. B*, vol. 78, no. 10, p. 104101, 2008.

[47] *Crystal-quasicrystal reconstructive phase transitions*. WORLD SCIENTIFIC, 2012.

[48] L. Landau, "Ld landau phys. z. sowjet, 11 (1937)," *JETP (Sov. Phys.)*, vol. 7, p. 627, 1937.

[49] L. D. Landau *et al.*, "On the theory of phase transitions," *Zh. eksp. teor. Fiz*, vol. 7, no. 19-32, 1937.

[50] P. Chandra and P. B. Littlewood, *A Landau Primer for Ferroelectrics*. Berlin, Heidelberg: Springer Berlin Heidelberg, 2007, pp. 69–116.

[51] A. Levanyuk, "Contribution to the theory of light scattering near the second-order phase transition points," *Zh. Eksp. Teor. Fiz.*, vol. 36, 1959.

[52] V. Ginzburg and V. Ginzburgm, "Some remarks on second order phase transitions and microscopic theory of ferroelectrics," *Fiz. Tverd. Tela*, vol. 2, no. 9, pp. 2031–2034, 1960.

[53] X. Granados, J. Fontcuberta, X. Obradors, L. Manosa, and J. B. Torrance, "Metallic state and the metal-insulator transition of $NdNiO_3$," *Phys. Rev. B*, vol. 48, no. 16, pp. 11 666–11 672, 1993.

[54] Y. Imry, "On the statistical mechanics of coupled order parameters," *Journal of Physics C: Solid State Physics*, vol. 8, no. 5, p. 567, 1975.

[55] G. Catalan, "Progress in perovskite nickelate research," *Phase Transitions*, vol. 81, no. 7-8, pp. 729–749, 2008.

[56] M. K. Stewart, C.-H. Yee, J. Liu, M. Kareev, R. K. Smith, B. Chapler, M. Varela, P. Ryan, K. Haule, J. Chakhalian, and D. N. Basov, "Optical study of strained ultrathin films of strongly correlated $LaNiO_3$," vol. 83, p. 075125, 02 2011.

[57] J. Ruppen, J. Teyssier, O. E. Peil, S. Catalano, M. Gibert, J. Mravlje, J.-M. Triscone, A. Georges, and D. van der Marel, "Optical spectroscopy and the nature of the insulating state of rare-earth nickelates," *Phys. Rev. B*, vol. 92, p. 155145, 2015.

[58] A. V. Boris, Y. Matiks, E. Benckiser, A. Frano, P. Popovich, V. Hinkov, P. Wochner, M. Castro-Colin, E. Detemple, V. K. Malik, C. Bernhard, T. Prokscha, A. Suter, Z. Salman, E. Morenzoni, G. Cristiani, H.-U. Habermeier, and B. Keimer, "Dimensionality control of electronic phase transitions in nickel-oxide superlattices." vol. 332, no. 6032, pp. 937–40, May 2011.

[59] A. D. Caviglia, R. Scherwitzl, P. Popovich, W. Hu, H. Bromberger, R. Singla, M. Mitrano, M. C. Hoffmann, S. Kaiser, P. Zubko, S. Gariglio, J.-M. Triscone, M. Först, and A. Cavalleri, "Ultrafast strain engineering in complex oxide heterostructures," *Phys. Rev. Lett.*, vol. 108, p. 136801, 2012.

[60] R. Scherwitzl, P. Zubko, I. G. Lezama, S. Ono, A. F. Morpurgo, G. Catalan, and J.-M. Triscone, "Electric-field control of the metal-insulator transition in ultrathin $NdNiO_3$ films," *Advanced Materials*, vol. 22, no. 48, pp. 5517–5520, 2010.

[61] A. Demourgues, F. Weill, B. Darriet, A. Wattiaux, J. Grenier, P. Gravereau, and M. Pouchard, "Additional oxygen ordering in" $La_2NiO_{4.25}$"($La_8Ni_4O_{17}$): II. structural features," *Journal of Solid State Chemistry*, vol. 106, no. 2, pp. 330–338, 1993.

[62] I. I. Mazin, D. I. Khomskii, R. Lengsdorf, J. A. Alonso, W. G. Marshall, R. M. Ibberson, A. Podlesnyak, M. J. Martínez-Lope, and M. M. Abd-Elmeguid, "Charge ordering as alternative to jahn-teller distortion," *Phys. Rev. Lett.*, vol. 98, p. 176406, 2007.

[63] S. J. Allen, A. J. Hauser, E. Mikheev, J. Y. Zhang, N. E. Moreno, J. Son, D. G. Ouellette, J. Kally, A. Kozhanov, L. Balents, and S. Stemmer, "Gaps and pseudogaps in perovskite rare earth nickelates," *APL Materials*, vol. 3, no. 6, pp. –, 2015.

[64] R. Rana, P. Pandey, V. E. Phanindra, S. S. Prabhu, and D. S. Rana, "Terahertz spectroscopic evidence of low-energy excitations in $NdNiO_3$," *Phys. Rev. B*, vol. 97, p. 045123, Jan 2018.

[65] D. G. Ouellette, S. B. Lee, J. Son, S. Stemmer, L. Balents, A. J. Millis, and S. J. Allen, "Optical conductivity of $LaNiO_3$: Coherent transport and correlation driven mass enhancement," *Phys. Rev. B*, vol. 82, p. 165112, Oct 2010.

[66] M. K. Stewart, D. Brownstead, J. Liu, M. Kareev, J. Chakhalian, and D. N. Basov, "Heterostructuring and strain effects on the infrared optical properties of nickelates," *Phys. Rev. B*, vol. 86, p. 205102, 2012.

[67] T. Katsufuji, Y. Okimoto, T. Arima, Y. Tokura, and J. Torrance, "Optical spectroscopy of the metal-insulator transition in $NdNiO_3$," vol. 51, pp. 4830–4835, Feb. 1995.

[68] R. Jaramillo, S. D. Ha, D. M. Silevitch, and S. Ramanathan, "Origins of bad-metal conductivity and the insulator-metal transition in the rare-earth nickelates," vol. 10, p. 304, 2014.

[69] S. Catalano, M. Gibert, V. Bisogni, O. E. Peil, F. He, R. Sutarto, M. Viret, P. Zubko, R. Scherwitzl, A. Georges, G. A. Sawatzky, T. Schmitt, and J.-M. Triscone, "Electronic transitions in strained $SmNiO_3$ thin films," *APL Materials*, vol. 2, no. 11, p. 116110, 2014.

[70] S. Catalano, M. Gibert, V. Bisogni, F. He, R. Sutarto, M. Viret, P. Zubko, R. Scherwitzl, G. A. Sawatzky, T. Schmitt, and J. M. Triscone, "Tailoring the electronic transitions of $NdNiO_3$ films through $(111)_{pc}$ oriented interfaces," vol. 3, 05 2015.

[71] A. B. Kuzmenko, D. van der Marel, F. Carbone, and F. Marsiglio, "Model-independent sum rule analysis based on limited-range spectral data," vol. 9, p. 229, Jul. 2007.

[72] B. Lau and A. J. Millis, "Theory of the magnetic and metal-insulator transitions in $RNiO_3$ bulk and layered structures," *Phys. Rev. Lett.*, vol. 110, no. 12, p. 126404, 2013.

[73] J. c. v. Chaloupka and G. Khaliullin, "Orbital order and possible superconductivity in $LaNiO_3/LaMO_3$ superlattices," *Phys. Rev. Lett.*, vol. 100, p. 016404, 2008.

[74] J. Rodríguez-Carvajal, S. Rosenkranz, M. Medarde, P. Lacorre, M. T. Fernandez-Díaz, F. Fauth, and V. Trounov, "Neutron-diffraction study of the magnetic and orbital ordering in $^{154}SmNiO_3$ and $^{153}EuNiO_3$," *Phys. Rev. B*, vol. 57, no. 1, pp. 456–464, 1998.

[75] V. Scagnoli, U. Staub, A. M. Mulders, M. Janousch, G. I. Meijer, G. Hammerl, J. M. Tonnerre, and N. Stojic, "Role of magnetic and orbital ordering at the metal-insulator transition in $NdNiO_3$," *Phys. Rev. B*, vol. 73, no. 10, p. 100409, 2006.

[76] V. Scagnoli, U. Staub, Y. Bodenthin, M. Garcia-Fernandez, A. M. Mulders, G. I. Meijer, and G. Hammerl, "Induced noncollinear magnetic order of Nd^{3+} in $NdNiO_3$ observed by resonant soft x-ray diffraction," *Phys. Rev. B*, vol. 77, no. 11, p. 115138, 2008.

[77] B. Torriss, J. Margot, and M. Chaker, "Metal-Insulator Transition of strained $SmNiO_3$ Thin Films: Structural, Electrical and Optical Properties," *Scientific Reports*, vol. 7, p. 40915, 2017.

[78] X. Granados, J. Fontcuberta, X. Obradors, and J. B. Torrance, "Metastable metallic state and hysteresis below the metal-insulator transition in $PrNiO_3$," *Phys. Rev. B*, vol. 46, pp. 15 683–15 688, 1992.

[79] I. Vobornik, L. Perfetti, M. Zacchigna, M. Grioni, G. Margaritondo, J. Mesot, M. Medarde, and P. Lacorre, "Electronic-structure evolution through the metal-insulator transition in RNiO$_3$," *Phys. Rev. B*, vol. 60, pp. R8426–R8429, Sep 1999.

[80] D. Kumar, K. P. Rajeev, J. A. Alonso, and M. J. Martínez-Lope, "Slow dynamics in hard condensed matter: a case study of the phase separating system NdNiO$_3$," *Journal of Physics: Condensed Matter*, vol. 21, no. 18, p. 185402, 2009.

[81] S. Lee, R. Chen, and L. Balents, "Landau theory of charge and spin ordering in the nickelates," *Phys. Rev. Lett.*, vol. 106, p. 016405, 2011.

[82] M. Hepting, M. Minola, A. Frano, G. Cristiani, G. Logvenov, E. Schierle, M. Wu, M. Bluschke, E. Weschke, H.-U. Habermeier, E. Benckiser, M. Le Tacon, and B. Keimer, "Tunable charge and spin order in PrNiO$_3$ thin films and superlattices," *Phys. Rev. Lett.*, vol. 113, p. 227206, 2014.

[83] H. Fujiwara, *Spectroscopic Ellipsometry: Principles and Applications*. John Wiley & Sons, 2007.